

## Chapter 2

# Analog Superconductivity Electronics

**Abstract** In this chapter we present results of achievement of modern analog superconducting electronics. In first section we discuss physical foundation and characteristics of superconducting edge bolometers. The influence of HTS materials on the characteristics is analyzed. Second section deals with description of samplers based on JJs. Two types of comparators-on single junction and balanced comparators are discussed. Presented results of linear theory for the estimation of time resolution of JJ comparators. Comparators using RSFQ technique discussed and ultimate characteristics presented. Third section is devoted to AC and DC SQUID magnetometers. Firstly, single and two-junction interferometers, the influence of d-wave order parameter symmetry on the characteristics are described. Furthermore, using these interferometers as sensitive elements of SQUIDs and characteristics is presented. Next section devoted to description of current state of superconducting microwave devices. Last topics in this chapter are using JJs in meteorology and description of multi-terminal superconducting devices.

### 2.1 Superconducting Bolometers

Superconducting bolometers is the *simplest devices* based on superconducting materials. It is well known, that the physical principle operation of the edge-transition bolometers is based upon the steep drop in their resistance,  $R$ , at critical temperature  $T_c$ . The bolometer converts the high-frequency current into an output signal at the frequency of modulation. Superconducting antenna bolometers can be used with various antennas, such as bow-tie, log-periodic or log-spiral. The main advantage of a superconducting bolometer is that since it operates as thermal detector it may be sensitive over a very wide electromagnetic spectrum. Antenna bolometers are characterized by several performance parameters. Some of these parameters are  $NEP$  (noise equivalent power), responsivity  $r$  and response time.  $NEP$  is defined in the same way as for any thermal detector. For a frequency band of  $1\text{Hz}$  it is given by Leonov and Khrebtov (1993)

$$(NEP)_{\min} = \frac{P_b^2}{\varepsilon} + \frac{4kT^2G}{\varepsilon^2} + \frac{4kT^2R}{S^2} + \frac{V_{1/f}^2}{S^2} + \frac{V_{amp}^2}{S^2}. \quad (2.1)$$

Where  $k$  is the Boltzmann constant,  $T$  is the bolometer temperature,  $P_b$  is the fluctuation power of background radiation,  $R$  is the bolometer resistance,  $\varepsilon$  is the absorption coefficient and  $G$  is the effective thermal conductance characterizing the thermal coupling between the bolometer and the heat sink. The first term is (2.1) is related with background radiation, the second term originates from the random energy exchange between the bolometer and the heat sink via the thermal conductance  $G$ . The third term takes into account the Johnson noise of the bolometer resistance, the fourth is determined by the excess voltage  $1/f$  noise  $V_{1/f}$  of a superconducting film. The fifth term is related with the contribution of the amplifier noise  $V_{amp}$ . As shown by estimation, at nitrogenim temperature  $T = 4K$  noise equivalent power  $NEP$  for LTS can be about  $(NEP)_{\min} = 10^{-14} \text{ Watt}/(\text{Hz})^{1/2}$  (Karmanenko et al. 2000).

Since the discovery of HTS, many works have been focused on the application of these materials in different types of bolometers for the near and far infrared wavelength regime (Fardmanesh and Askerzade 2003; Bozbey et al. 2003). The responsivity versus modulation frequency and versus the temperature of superconducting bolometers has previously been investigated and reported in Leonov and Khrebtov (1993). A simple  $RC$ -model for the amplitude of bolometric response results in the following expression (Fardmanesh 2001)

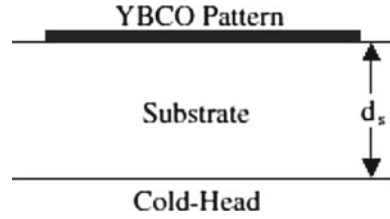
$$r = \frac{\varsigma I}{G(1 + j\omega\tau)} \frac{dR}{dT}, \quad (2.2)$$

where  $\tau = C/G$ ,  $I$  is the DC bias current,  $\varsigma$  is the fraction of the incident power absorbed by the bolometer,  $\omega$  is the modulation frequency,  $r$  is the frequency-dependent responsivity in units of  $VW^{-1}$ , and  $G$  and  $C$  are the thermal conductance and the heat capacity of the bolometer, respectively. As shown in (2.2), thermal conductance  $G$  is a major parameter in the amplitude of the response function. According to (2.2) the temperature-dependent phase of the response can be calculated by the equation

$$\tan \theta = -\frac{\omega C}{G}. \quad (2.3)$$

It is important to understand the factors that determine  $G$  and  $C$  of the bolometers as a function of the temperature, frequency and other parameters of the bolometer configuration. In the study (Bozbey et al. 2003) developed thin-film YBCO on crystalline  $MgO$  bolometers. Below presented on the phase of the response to infrared signal of the edge-transition bolometers versus temperature at high and low modulation frequencies. In study (Karmanenko et al. 2000) it was proposed a model that can explain the observed discrepancy in the measured response versus temperature compared to that expected from other models. According to presented model, the thermal constants  $G$  and  $C$  change as a film goes into the superconducting state. This might also partly be accounted for some observed non-bolometric component of the response in these types of bolometers.

**Fig. 2.1** Sample configuration of YBCO based bolometer ( $d_s$  is substrate thickness)



The typical configuration of the studied samples is shown in Fig. 2.1. A sample holder was designed and made of high purity and high conductive oxygen-free copper. The heater is made of resistive paste on a sapphire substrate using hybrid microelectronics technology and can control the temperature with a DC current up to maximum of about 200 mA with a precision of 0.1 K. As shown in Fig. 2.1, there are two thermal boundary resistances at the substrate interfaces, one at the film interface and the other at the holder interface. There are also two major bulk areas which constitute the overall heat capacity of the samples, one due to the superconducting film and the other due to the substrate material. The thickness of the superconducting YBCO film was about 200 nm. The phase and magnitude of the response versus temperature at different frequencies were measured using a lock-in amplifier. A light emitting diode with a peak radiation wavelength of about  $0.85 \mu\text{m}$  was used as the radiation source for the response versus modulation frequency studies in all the measurements. In analyzing the different operation regimes of the edge-transition bolometer parameters, the frequency dependence of the thermal diffusion length plays an important role. It is well known that thermal diffusion length into substrate,  $L_f$ , is determined as Hu and Richards (1989), Hwang et al. (1979)

$$L_f = \left( \frac{D}{\pi f} \right)^{1/2}, \quad (2.4)$$

where  $D = K/C$  is the thermal diffusivity of the substrate material, and  $K$  and  $C$  are the thermal conductivity and specific heat (per unit volume) of the substrate material, respectively. At high chopping frequencies,  $L_f$  becomes comparable to or smaller than the substrate thickness changing  $G$ . Then  $G$  is limited by the thermal conductance of the substrate material and can be obtained from

$$G = \frac{KA}{L}, \quad (2.5)$$

where  $L$  and  $A$  are the thickness of the substrate and the area of the superconducting pattern, respectively.

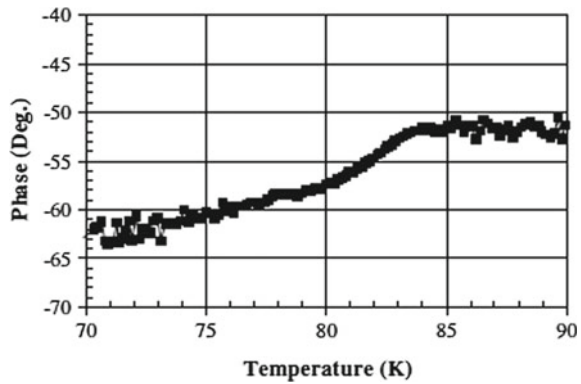
The phase of the response of the samples is found to be more sensitive to the values of the characteristic parameters of the bolometers than the magnitude of the response. The phase of the response has shown a strong variation as the sample goes through the normal–superconducting transition both at low and high modulation

frequencies also showing modulation frequency dependence. At low frequencies, the phase of the response starts to decrease as the temperature decreases below about the onset temperature of the normal to superconducting transition (i.e., at  $T < T_{c-onset}$ ). Opposite behaviour has been observed at high modulation frequencies, i.e. the phase of the response starts to decrease at  $T < T_{c-onset}$ . This clearly indicates that large changes in the phase and magnitude of response are mainly associated with the differences in the conduction mechanisms in the normal and superconducting states, rather than the well-known temperature dependence of the interface boundary resistance.

### 2.1.1 Low Frequency Limit

At low modulation frequencies the phase of the response versus temperature increases by decreasing the temperature starting at  $T < T_{c-onset}$  as shown in Fig. 2.2. The respective amplitude of the response normalized to the measured  $dR/dT$  of the superconducting film at  $T < T_{c-onset}$  for low modulation frequencies is shown in Fig. 2.3. The amplitude of the response in Fig. 2.3 increases above the expected value determined by the  $dR/dT$  of the film as the temperature is lowered towards the  $T_{c-zero}$ . Such behavior would be consistent with a decrease of the thermal conductance of the bolometer. The variation of the heat capacity at low temperatures, reveals typical  $T^3$  dependence behavior (Barron et al. 1959). At low modulation frequencies ( $\omega = 20\text{ Hz}$ ), the thermal conductance in the studied samples is determined by the substrate/cold-head interface conductance, or the so called Kapitza boundary resistance, caused by the acoustic mismatch impedances of the interfaced materials (Fardmanesh 2001). According to (2.4), by lowering the frequency the thermal diffusivity length into the substrate becomes longer than the substrate thickness and phonons emitted by the superconducting film into the substrate will reach the substrate/cold-head boundary. The observed thermal boundary conductance at

**Fig. 2.2** Phase of the response versus temperature at low modulation frequency 20 Hz and 680  $\mu\text{A}$



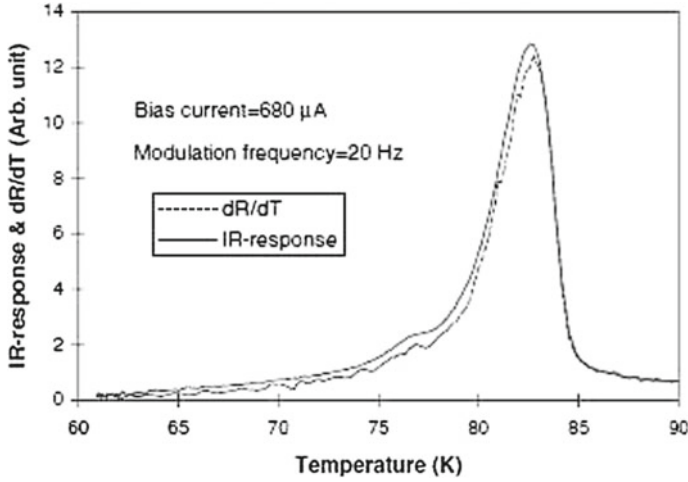


**Fig. 2.3** Amplitude response versus temperature at modulation frequency 20 Hz and 680  $\mu\text{A}$

the substrate/cold-head interface can be explained by the theory of Kapitza conductance. It is well known that Kapitza conductance is the derivative of the net heat flux transmitted across an interface with respect to the temperature difference between the two materials (Swartz and Pohl 1989). Therefore, if we consider an interface between materials  $A$  and  $B$ , we can write  $G_K$  as

$$G_K = \frac{1}{V} \frac{\partial}{\partial T} \sum_k \sum_j^A \hbar \omega_{kj} n(\omega_{kj}, T) v_{kz} t_{kj} = \frac{1}{V} \frac{\partial}{\partial T} \sum_k \sum_j^B \hbar \omega_{kj} n(\omega_{kj}, T) v_{kz} t_{kj}, \quad (2.6)$$

where the labels  $A$  and  $B$  on the sums indicate that all quantities in each sum correspond to phonons incident on the interface from the materials  $A$  and  $B$  sides, respectively. In Eq. (2.6),  $\omega_{kj}$  is the phonon frequency,  $v_{kz}$  is the component of the phonon group velocity normal to the interface,  $n(\omega_{kj}, T)$  is the Bose–Einstein distribution function,  $t_{kj}$  is the probability that a phonon of wave vector  $k$  and polarization  $j$  will be transmitted across the interface between materials  $A$  and  $B$ , and  $V$  is the volume. The Kapitza conductance can be calculated at low temperatures ( $\hbar \omega_D / kT \gg 1$ ) analytically taking into account Debye phonon density of states, which can be obtained from

$$D(\omega) = \frac{1}{V} \sum_{kj} \sum_j \delta(\omega - \omega_{kj}) = \frac{\omega^2}{2\pi^2 c^3}, \quad (2.7)$$

where  $c$  is the velocity of sound in the material. As a result of calculations, the thermal conductance has  $T^3$  characteristics at low temperatures and remains constant at high temperatures. The phonon system in each material in the

above calculations is considered to be of the equilibrium nature. However, in the calculation of the boundary conductance of the substrate/cold-head interface we should take into account the phonon density of the state spectrum of the non-equilibrium phonons, which propagate into the *MgO* substrate and reach boundary substrate/cold-head (the diffusion regime of propagation of phonons). Hence, one should determine the differences in the photo-absorption process in normal and superconducting states. As shown by the analysis of thermalization and photoabsorption in YBCO superconductors (Bluzer 1991), interaction between hot quasi-particles and Cooper pairs condensate continues to divide the excess energy by forming three quasiparticles. The hot quasi-particles continue to break additional pairs by the electron–electron interaction process as they thermalize toward the energy gap by discrete energy steps. As a result we have a characteristic feature—a jump at frequency  $\omega = 2\Delta(T)$  due to the activation of the recombination mechanism of phonon generation (Chang and Scalapino 1977) (for  $\omega < 2\Delta(T)$ , phonons are generated as a result of the energy relaxation of high energy quasi-particles). The phonon distribution function (product of  $D(\omega)n(\omega, T)$ ) has fairly narrow maximum near  $\omega = 2\Delta(T)$  (Sergeev and Reizer 1996), i.e. in our calculation we should replace Debye phonon density of states by the Einstein phonon density function

$$D(\omega) = \omega^2 \delta(\omega - 2\Delta(T)). \quad (2.8)$$

Assuming that transmission probability and normal component of the group velocity to the interface to be independent of temperature, Eq. (2.6) can be rewritten as

$$G_K = \frac{1}{V} \sum_j^A \int_0^{\omega_{\text{Debye}}} d\omega \hbar \omega_{kj} D(\omega) \frac{dn(\omega_{kj}, T)}{dT} v_{kjz} t_{kj}, \quad (2.9)$$

where for  $dn(\omega, T)/dT$  we have the following expressions:

$$\frac{dn(\omega_{kj}, T)}{dT} = \left\{ \begin{array}{l} \frac{k}{\hbar\omega}, \frac{\hbar\omega}{kT} \ll 1 \\ \frac{k}{\hbar\omega} x^2 \exp(-x), x = \frac{\hbar\omega}{kT} \gg 1 \end{array} \right\}. \quad (2.10)$$

It is clear that at high phonon frequencies,  $2\Delta(T)$  is about the equilibrium temperature of the substrate  $T$  and the contribution of the non-equilibrium phonons to the heat transfer has exponential behavior. As shown by the above calculations, at temperatures close to critical temperature  $2\Delta(T) \ll T_c$ , where  $\Delta(T) = \Delta_0(1 - T/T_c)^{1/2}$  (standard BCS theory), low frequency phonons do not influence heat transfer process and boundary conductance at substrate/cold-head. Hence, the calculated normalized conductance based on expressions (2.9) and (2.10) are in good agreement with the experimental data for the thermal conductance versus temperature at low modulation frequency. The discrepancy between the experimental data and calculations at temperatures close to  $T_c$  shown in Fig. 2.4 is interpreted to be associated with the tendency of the emitting phonon frequency to zero. Here we also consider superconducting materials without magnetic flux quantum. It is clear that temperatures close

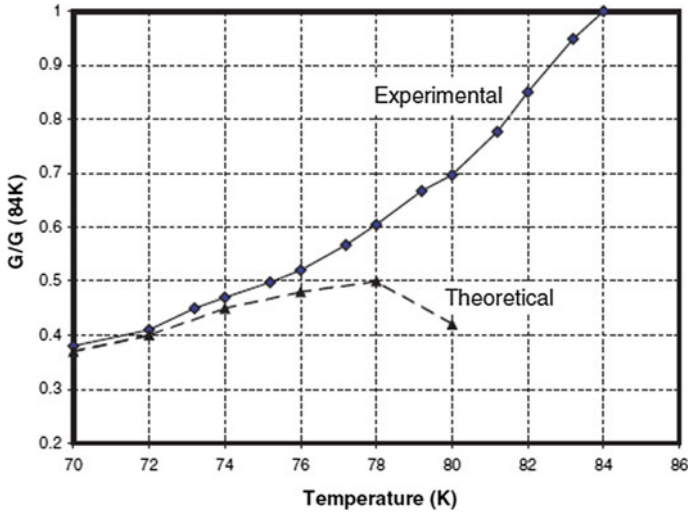


**Fig. 2.4** Temperature dependence of normalized Kapitza resistance of bolometer

to the  $T_c$  can easily lead to Abrikosov vortices in the films. In the equilibrium, flux quanta are present in the film and move due to the thermal activations. The optical photons also create additional magnetic flux quantum and the flux motion (creep and flow). This factor can lead to the non-bolometric component in the optical response, not considered in the above calculations. In our opinion, discrepancy between theory and experiment can also be related to flux dynamics near  $T_c$ . This argument is suggested by the experimental data from Fardmanesh (2001). As shown in this paper, for the samples with sharper transition, the change in the phase of the response and the discrepancies at low frequencies are smaller. One of the possible reasons for the broadening of the transition into a superconducting state is the penetration of flux quantum into the samples. Another possible improvement of presented model is connected with using realistic behavior of the order parameter close to  $T_c$  and d-wave characteristics of the pairing in YBCO compounds. On the other hand, influence of the order parameter relaxation near  $T_c$  on the bolometer characteristic should also be taken into account for more accurate calculations near critical temperature.

### 2.1.2 High Frequency Limit

The variation of the phase of the response versus temperature at high modulation frequency (e.g.,  $\omega = 10$  kHz) is shown in Fig. 2.5. At frequencies above the knee frequency,  $f_L$ , the phase of the response decreases as the temperature is lowered. To describe the heat transfer in this regime we imply the phonon radiation limit (Bluzer 1991) (ballistic regime of propagation of phonons). In the high-frequency

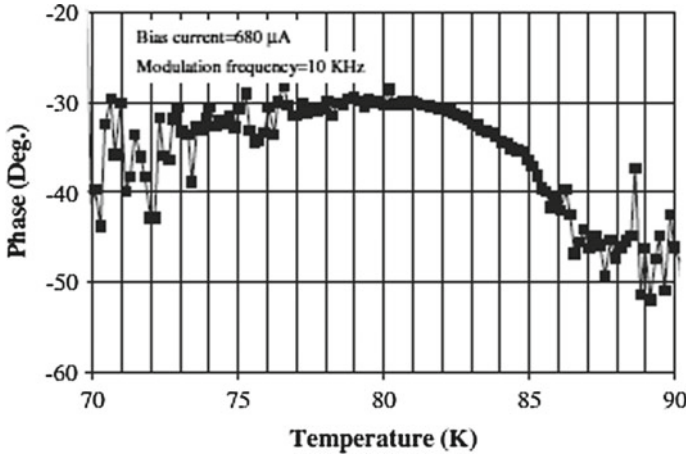


**Fig. 2.5** Phase of the response versus temperature at high modulation frequency 10 kHz and 680  $\mu\text{A}$

regime, all phonons from the superconducting film are assumed to transmit across the film–substrate boundary and absorbed in the substrate media. That is, in Eq. (2.6), transmission probability  $t_{kj}$  can be considered 1. Such approximation is valid due to the low Kapitza resistance of the film–substrate boundary (Hu and Richards 1989). As shown by calculations (Richardson et al. 1992), the thermal conductivity in HTS films has different behavior in contrast to conventional LTS. In cuprate compounds, thermal conductivity below  $T_c$  versus temperature has a peak near the  $T_c$  which is lowered by decreasing the film thickness (Richardson et al. 1992). The thermal conductance of the studied devices at high modulation frequencies is previously shown to be mainly governed by thermal conductivity of the substrate material taking into account the processes in superconducting film (Hu and Richards 1989). The thermal conductivity of the substrate can also increase as the temperature decreases below the  $T_{c-onset}$ . This is due to enhancement of the mean-free path of phonons emitted from the superconducting film into the substrate. As a result, the phase of the response in the temperature interval  $75\text{ K} < T < 85\text{ K}$  decreases and at lower temperatures,  $T < 75\text{ K}$ , increases. The corresponding amplitude of the response at high frequencies is shown in Fig. 2.6. Response at temperatures  $T < 75\text{ K}$  can be closer to the  $dR/dT$  curve. The discrepancy in amplitude of response in the temperature interval  $75\text{ K} < T < 85\text{ K}$  is interpreted to be related to the variation of the thermal conductivity in the substrate material.

## 2.2 Superconducting Samplers

The considerable nonlinearity of the IV curve of JJs makes them promising for digital and pulsed devices (Hamilton et al. 1981; Hayakawa 1983). Super-high-speed switches have been built around complex distributed JJs and interferometers, where



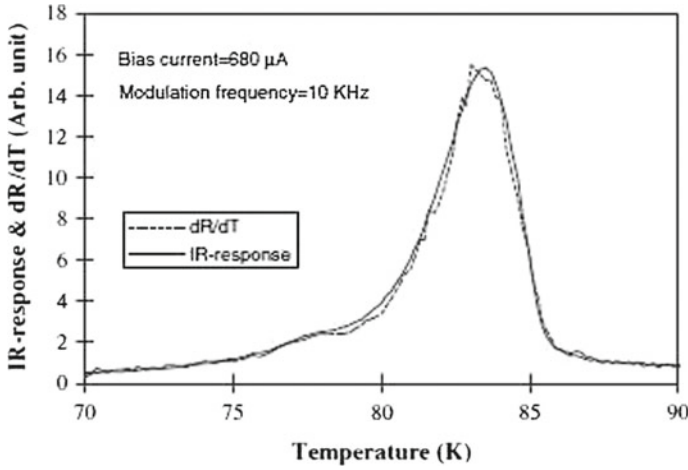


**Fig. 2.6** Amplitude response versus temperature at modulation frequency 10 kHz and 680  $\mu$ A

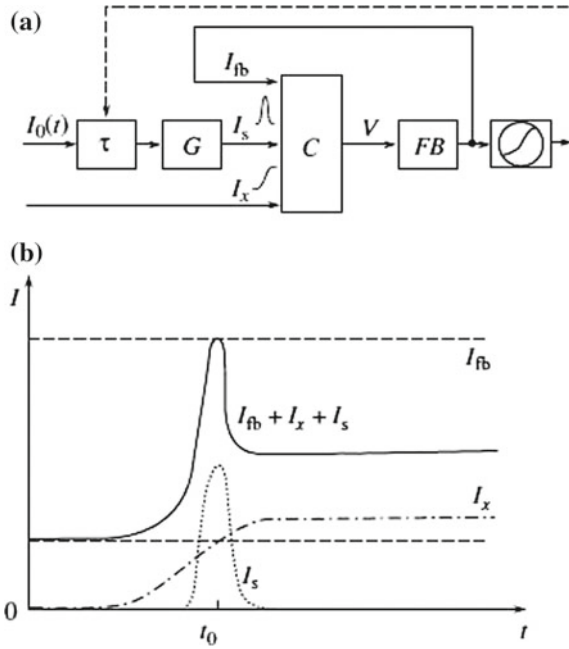
switching is induced by suppressing the critical current of the system (Zappe 1975; Fulton et al. 1977). Switching cells on JJs can be viewed as building blocks for samplers. These devices make it possible to display the waveform of weak ultrashort (picosecond) pulses (Wolf et al. 1985a; Akoh et al. 1983). The schematic of a comparator sampler is shown in Fig. 2.7a; the signal waveform and the operation of the device, in Fig. 2.7b. The basic element here is comparator  $C$  with distinct operating threshold  $I_t$ .

A pulse to be measured  $I_s(t_0)$ ; short strobe  $I_x(t-\tau)$  of fixed amplitude and duration; and slowly varying feedback signal  $I_{fb}$  are simultaneously applied to the comparator. If sum  $I_{fb} + I_x + I_s$  exceeds threshold, the comparator switches, generating an output pulse of high fixed amplitude  $V$  and appreciable duration  $T_0$ . Feedback loop (FB) adjusts current so that the equality

$$I_{fb} + I_x(t_0) + I_s(t_0) = I_t \quad (2.11)$$

is fulfilled. Then, using signal  $I_{fb}$ , one can find  $I_x$  at instant  $t_0 = t + \tau$  the strobe reaches a maximum. This short strobe is formed by generator  $G$  from reference pulse  $I_0(t)$  delayed by time. Slowly varying this delay, one can record the waveform of  $I_x$ . It should be noted that semiconducting samplers use another, selection/storage, approach to measure weak signals. The operation and performance of semiconductor samplers are detailed in Ryabinin (1968). A superconducting analogue to the selecting/storing device has not been found yet. The aim of this section is to review the advances in superconducting electronics in the field of Josephson comparator samplers. This issue is also topical in the light of discovery of new superconducting compounds, such as HTS (Bednorz and Muller 1986), magnesium diboride  $\text{MgB}_2$  (Nagamatsu et al. 2001) and Fe-based superconductors (Askerzade 2012). Contrary

**Fig. 2.7** a Block diagram of comparator sampler b Operation of JJ comparators

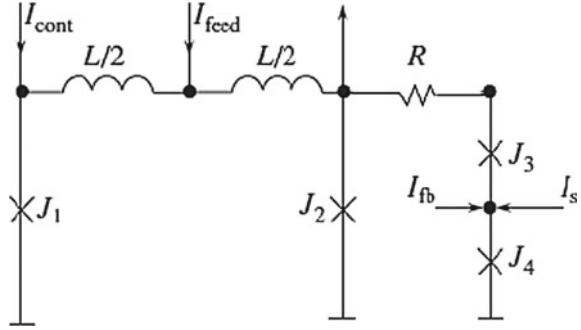


to the early expectations,  $\text{MgB}_2$  is now viewed as a superconductor capable of replacing LTS counterparts. To estimate the potential of the new superconductors as the material for samplers, it is necessary to theoretically determine their associated time resolution  $\delta t$  and sensitivity  $\delta I_x$ .

### 2.2.1 Comparators on Single JJ

Early superconducting samplers were based on two tunnel JJs, one of which served as a generator of short strobes and the other as a comparator. Such a design of the sampler was proposed in Faris (1980). The basic circuit of this comparator is shown in Fig. 2.8. It consists of JJ  $J_4$ , which is connected to an interferometer based on two JJs  $J_1$  and  $J_2$  through resistor  $R$  and shaper  $J_3$ . Switching of the interferometer is accomplished by appropriately selecting feed current  $I_{feed}$  and control current  $I_{cont}$ . A pulse steep edge that is observed when the interferometer is switched into the resistive state becomes still steeper under the action of small junction  $J_3$ . As a result, a short strobe is formed, which is applied to comparator  $J_4$ , where it adds up with signal current  $I_3$  and feedback current  $I_{fb}$ . Once the critical current has been exceeded, the JJ switches into the resistive state and, accordingly, the feedback current changes.

**Fig. 2.8** JJ based comparator on  $J_4$  ( $J_1$  and  $J_2$  presents two-junction interferometer,  $J_3$  is the sharper for strobe-pulses)



The dynamics of the circuit shown in Fig. 2.8 was simulated and analyzed in detail in paper (Askerzade 2000a). Using the PSCAN (Personal Superconductive Circuit ANalyzer) software package developed in Moscow State University (Polonsky et al. 1991), the shape of the strobe versus feed current  $I_{feed}$  and McCumber parameter  $\beta_C = \frac{2\pi I_c R_N^2 C}{\Phi_0}$  was studied and strobe rise time isolines on the parameter plane ( $I_{feed}$ ,  $\beta_C$ ) were constructed (Askerzade 2000a). It was shown that, for JJs with  $\beta_C < 3$ , the circuit shown in Fig. 2.8 becomes inappropriate because of a distortion of the strobe shape. The oscillation amplitude at the tail of strobe increases, becoming comparable to the “core” of the pulse (Askerzade 2000a). Such a conclusion comes into conflict with the results of Wolf et al. (1985a), where it was argued that a picosecond time resolution may be reached by further growing of current density, i.e. by lowering  $\beta_C$ .

### 2.2.2 Time Resolution of a Single-Junction Comparator

The time resolution of the Josephson comparator is fundamentally limited by its inertial properties. According to Likharev et al. (1990), this parameter for a single JJ comparator can be roughly estimated by the expression

$$\Omega_p(0)t = \frac{1}{(1 - \frac{I_t}{I_c})^{1/2}}, \quad (2.12)$$

where

$$\Omega_p^2(0) = \frac{2eI_c}{\hbar C} = \frac{2ej_c t_i}{\hbar \epsilon \epsilon_0}. \quad (2.13)$$

is the plasma frequency of a tunnel JJ (see also Eq. 1.67) (Likharev 1986),  $t_i$  is the thickness of an insulating spacer between the superconductors,  $\epsilon$  is the permittivity, and  $\epsilon_0$  is the dielectric constant. In expression (2.12), ratio  $I_t/I_c$  characterizes the proximity of the real threshold of action of the comparator, to its critical current  $I_c$ . Under the actual conditions of thermal fluctuations,  $1 - I_t/I_c$  is on the order of

$\gamma_T^{1/3}$ , where  $\gamma_T$  is the ratio of thermal energy  $kT$  to Josephson energy  $E_J = \frac{\hbar I_c}{2e}$ ,  $\gamma_T = \frac{kT}{E_J} = \frac{2ekT}{\hbar I_c}$  (Likharev 1986). For JJs based on LTS,  $\gamma_T$  can be set equal to 0.01. If  $V_c = 2$  mV, which is typical of commonly used LTS (Nb, Pb),  $\delta t = 3$  ps. Nearly the same values of the time resolution were obtained in Wolf et al. (1985a) for Pb-based junctions. It was noted in the introduction to this chapter, that a strobe pulses must have a fixed amplitude and duration. However, thermal and fabrication-induced fluctuations in the circuit of a two-junction interferometer make these parameters and, hence, the performance of samplers unstable.

### 2.2.3 Dynamics of Balanced Josephson Comparator

An important step toward improving the performance of superconducting samplers is to raise their stability against noise and temperature fluctuations. To this end, it was suggested that JJs be configured into a Goto pair to form a balanced scheme (Bakhtin et al. 1983; Kornev and Semenov 1987). Here, two identical junctions are connected in series relative to a strobe signal and in parallel relative to a signal to be measured. The operation of the Goto pair has long been known and is applied, e.g., in semiconductor samplers based on Esaki diodes (Karklinsh and Khhermanis 1980). One more advantage of balanced comparators is that distortions due to the nonideality of a strobe pulses are eliminated.

The circuit presented in Fig. 2.8 is easily converted to a balanced circuit if junctions  $J_3$  and  $J_4$  are made identical. To study the dynamics of a balanced comparator on JJs, it is necessary to construct the switching characteristic of the comparator on the plane  $(\frac{dI}{d\tau}, I_s)$ , where  $\frac{dI}{d\tau}$  is the rate of strobe current and  $I_s$  is the signal current. The switching characteristic is constructed as follows: as rate of rise  $\frac{dI}{d\tau}$  grows, the signal current must be increased so that, for switching time  $R_N C$  of the first junction, the current through the second junction does not reach critical value  $I_c$ , which means

$$\frac{dI}{d\tau} R_N C < I_s. \quad (2.14)$$

Another way of designing balanced comparators around tunnel JJs is the use of an internal clock generator as a strobe pulse (Askerzade and Kornev 1994b). The dynamics of related processes was numerically simulated with the PSCAN software package (Polonsky et al. 1991). It was found (Askerzade 2000b) that both junctions are switched into the resistive state when the signal is low. The time resolution approaches its fundamental limit if sampling rate is too low, which is observed when  $\alpha\beta_C < \delta i$  with  $\delta i$  is the fluctuation smearing of the comparator's threshold characteristic. It is well known that fluctuation smearing  $\delta i = \frac{I_T}{I_c}$  (Likharev 1986), where critical current  $I_c$  varies usually between 10  $\mu$ A–1 mA for tunnel junctions in LTS. At liquid-helium temperature,  $I_T \approx 0.3$   $\mu$ A; for liquid-nitrogen temperature,  $I_T$  may reach 32  $\mu$ A.

The dynamics of a two-junction interferometer can be used to reduce distortions in the shape of the strobe pulse and obtain very short single flux quantum (SFQ)

pulses. Taking  $I_{feed}$  (Fig. 2.8) below the threshold value and appropriate  $I_{cont}$ , one can generate a SFQ pulse of area

$$\int V dt = \Phi_0 = 2 \text{ mV} \times \text{ps} \quad (2.15)$$

amplitude of about  $2V_c$ , and duration of  $\frac{\pi}{\omega_c}$ . Such an approach, however, requires that a latching source be used. In this case, it is convenient to apply a generator of RSFQ pulses that is built around a single JJ with a hysteresis-free IV curve (Kornev and Semenov 1987; Gudkov et al. 1988).

### 2.2.4 Time Resolution of Balanced Tunnel Josephson Comparators

As for any sampler, the time resolution of the given device can be determined using the transfer characteristic  $H(\tau)$  (Karklinsh and Khermanis 1980), which relates the output signal of a sampler,  $V_{out}$ , to a signal applied to the input of the comparator in the form of a small step,  $I_s = I\theta(t)$ . The time resolution is defined as the time taken for the characteristic  $H(\tau)$  to rise from 10 to 90% of its maximal value, where  $\tau$  is the delay (advance) time of the strobe pulses relative to the time the step is applied to the input of the comparator. For identical JJs  $J_3$  and  $J_4$  (Fig. 2.8), the following phase relationships are valid:

$$\beta_C \ddot{\phi}_3 + \dot{\phi}_3 + \sin \phi_3 = i_0, \quad (2.16)$$

$$\beta_C \ddot{\phi}_4 + \dot{\phi}_4 + \sin \phi_4 = i_0 + i_1. \quad (2.17)$$

Here,  $i_0$  and  $i_1$  are the currents in units of the JJ critical current ( $i_0$  is the strobe-induced current, and  $i_1$  is the sum of the feedback and signal currents);  $\tau$  is given in units of  $\Phi_0/2\pi I_c R_N$ ;  $\Phi_0$  is the flux quantum, and  $R_N$  is the JJ resistance in the normal state. For small deviations of the phase relative to the strobe pulses,  $\delta\phi = \phi_3 - \phi_4$ , we have

$$\beta_C \delta \ddot{\phi} + \delta \dot{\phi} + \cos\left(\frac{\phi_+}{2}\right) \delta \dot{\phi} = i_1, \quad (2.18)$$

$$\beta_C \frac{\phi_+}{2} + \frac{\phi_+}{2} + \sin \frac{\phi_+}{2} = i_0, \quad (2.19)$$

where  $\phi_+ = \phi_3 + \phi_4$ . An asymptotic solution of Eq. (2.19) in the case of a linearly growing sampling current through a JJ,  $i_0 = \alpha\tau$ , is given in Likharev (1986) and Snigirev (1984) (In this section  $\alpha$  denotes the sampling rate.)

$$\frac{\phi_+}{2} = \frac{\pi}{2} + \left\{ \begin{array}{ll} -\sqrt{-2\alpha(\tau - \alpha^{-1})}, & \text{at } \phi_+ \rightarrow -\infty \\ u_0(\tau - \alpha^{-1} - \tau_0) & \text{at } \phi_+ \simeq 0 \\ \frac{12\beta_C}{(\tau - \alpha^{-1} - \tau_d)^2} & \text{at } \phi_+ \rightarrow \infty \end{array} \right\}, \quad (2.20)$$

where  $u_0 = 1.64\alpha^{3/5}\beta_C^{-1/5}$  and  $\tau_0 = 0.95\alpha^{1/5}\beta_C^{-1/2}$ . The mean delay time  $\tau_d$  is given by

$$\tau_d = 4.64\alpha^{-1/5}\beta_C^{2/5}. \quad (2.21)$$

Let  $i_s = \Theta(t - \tau)$  be the input signal in the form of Heaviside step function at time instant  $t = \tau$ . Then, the solution to Eq. (2.18) has the form

$$\delta\phi = \int_{-\infty}^t K(t, \xi) [\Theta(t - \xi) + i_b(\tau)] d\xi. \quad (2.22)$$

If  $\beta_C\alpha \ll 1$ , the kernel in case of a linearly growing current,  $i_0 = \alpha\tau$ , has the form

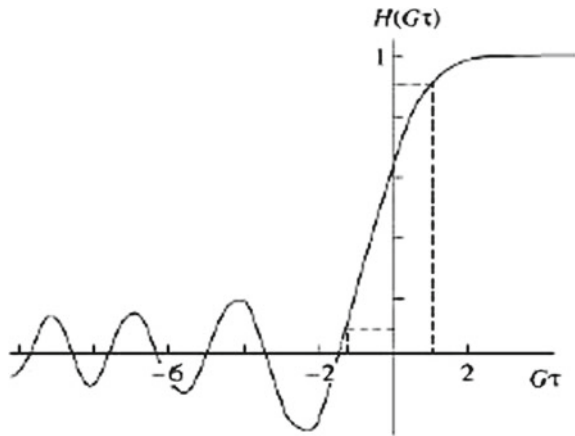
$$K(t, \xi) = \pi Ai(G\xi)Bi(Gt), \quad (2.23)$$

where  $Ai(\dots)$  and  $Bi(\dots)$  are the Airy functions and  $G = 1.14^{1/3}\alpha^{1/5}\beta_C^{-1/5}$ . For any  $\tau$ , transfer characteristic  $H(\tau)$  obtained from the condition of nongrowing solution has the form

$$H(t) = H_0^{-1} \int_{-\infty}^t d\xi Ai(G\xi); \quad H_0 = \int_{-\infty}^{\infty} dt Ai(Gt). \quad (2.24)$$

Figure 2.9 shows that the transfer characteristic of a balanced comparator based on tunnel JJs is of oscillatory character at  $\tau < 0$ . Such behavior is associated with a complete set of reactances in the equivalent circuit of a JJ at  $\beta_C \gg 1$  (see Fig. 1.19) (Likharev 1986). From Fig. 2.9, we find that the time resolution of tunnel JJ

**Fig. 2.9** Transfer characteristic of a balanced tunnel JJ comparator



comparators is

$$\delta t = 2.3\alpha^{-1/3}\beta_C^{2/5}. \quad (2.25)$$

As follows from last equation, time resolution  $\delta t$  depends on capacitance  $\beta_C$  of a JJ and sampling rate  $\alpha$  of the strobe-induced current through the junction. A pair of tunnel JJs ceases to operate as a comparator when  $\alpha\beta_C < \frac{I_T}{I_c}$ . Under the assumptions made above, the time resolution is estimated at a level of several tens of picoseconds. This means that, for slow strobes, the time resolution is far from the limiting value of the superconducting devices (Wolf et al. 1985a). Thus, it is necessary either to reject the balanced tunnel scheme of a Josephson comparator and use unbalanced designs or to design balanced comparators on hysteresis-free (overdamped) JJs, which are considered next section.

### 2.2.5 Balanced Comparators on Overdamped JJs

Figure 2.10 shows the equivalent circuit of a development a device that handles RSFQ idea (Kornev and Semenov 1987; Gudkov et al. 1988). JJ  $J_1$  shunted by resistor  $R_1$  generates flux quanta with a repetition rate that is proportional to mean voltage  $V_1$  across this junction and is controlled by bias current  $I_1$ , which far exceeds its critical current  $I_c$ . RSFQ pulses acting as strobes enter a buffer discrete transmission line made of JJs  $J_2$ – $J_4$ . The output of this line is connected to a balanced comparator on Josephson pair  $J_6$  and  $J_7$  through junction  $J_5$ . Bias currents  $I_2$  and  $I_3$  of the Josephson transmission line (JTL) and comparator are lower than the critical current of these junctions. When such a device is used as the pulsed comparator of a sampler, the output signal is mean voltage  $V_{av}$  across JJ  $J_7$  (or  $J_6$ ), which is proportional to the probability that a single flux quantum escapes loop  $J_4$ – $J_7$  precisely from this junction. Current  $I_4$  is a sum of the current to be measured,  $I_s$ , and feedback current  $I_{fb}$ . The feedback makes current  $I_4$  equal to threshold current  $I_t$  when the probability of a RSFQ pulses escaping is 0.5. The output voltage of the sampler,  $V_{out}$ , is proportional

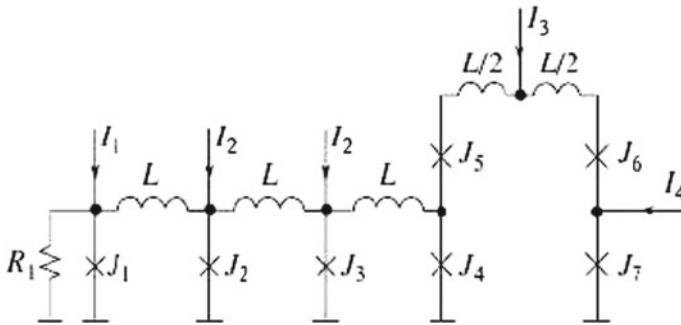


Fig. 2.10 Equivalent representation of RSFQ circuit developed in Gudkov et al. (1988)

to  $I_{fb}$ . The dynamics of a balanced comparator on overdamped JJs was analyzed in detail in papers (Gudkov et al. 1988; Snigirev 1984; Askerzade et al. 1990; Askerzade and Kornev 1994a).

### 2.2.6 Time Resolution of Balanced Overdamped Josephson Comparators

Here, we will use the same dynamic equations (Eqs. (2.16) and (2.17)) as for tunnel junctions. Since the McCumber parameter is small,  $\beta_C \ll 1$ , the first terms in these equations are ignored. For the circuit in Fig. 2.10, the indice for the Josephson phases are changed and, for a linearly growing current through a overdamped junction, we have

$$\frac{\phi_+}{2} = \frac{\pi}{2} + \left\{ \begin{array}{ll} -\sqrt{-2\alpha(\tau - \alpha^{-1})}, & \text{at } \phi_+ \rightarrow -\infty \\ u_0(\tau - \alpha^{-1} - \tau_0) & \text{at } \phi_+ \simeq 0 \\ \frac{2^{1/3}}{(\tau - \alpha^{-1} - \tau_d)^{1/3}} & \text{at } \phi_+ \rightarrow \infty \end{array} \right\}, \quad (2.26)$$

here  $u_0 = 1.64\alpha^{3/5}$  and  $\tau_0 = 1.21\alpha^{-1/3}$ . The mean delay time  $\tau_d$  is given by

$$\tau_d = 2.9\alpha^{-1/3}. \quad (2.27)$$

Using the solution

$$\delta\phi = \int_{-\infty}^t \exp\left(-\frac{\phi_+(x)dx}{2}\right) \int_{-\infty}^t [\Theta(t - \xi) + i_{fb}(\tau)] d\xi. \quad (2.28)$$

and the Eq. (2.26), we obtain, upon integration, an expression for the transfer characteristic  $H(\tau)$

$$H(\tau) = 1 - \operatorname{erf} \left\{ \sqrt{\frac{1.25}{2}} \alpha^{1/3} \tau \right\} \quad (2.29)$$

where  $\operatorname{erf}(\dots)$  is the error integral. Then, using tabulated data for the error integral, one can estimate the time resolution of balanced overdamped comparators as

$$\delta t = 0.64 \frac{\Phi_0}{2\pi I_c R_N}. \quad (2.30)$$

When deriving of expression (2.30), we assumed that a SFQ pulse has a triangular shape and so the sampling rate can be written as  $\alpha = 2/\pi$ . For real values of the characteristic voltage  $V_c = I_c R_N = 2 \text{ mV}$ , the time resolution is about 1 ps. The above analysis is referred to the case when a pulsed comparator is based on a Goto pair. Actually, however, the behavior of this system is more complicated (Askerzade and Kornev 1994a); specifically, the effect of inductance in the circuit is disregarded



in the analysis given above. Therefore, the process dynamics in this circuit was numerically simulated in the absence of fluctuations (Askerzade and Kornev 1994a) in order to see how phases  $\phi_6$  and  $\phi_7$  of respective JJs of the balanced comparator vary when a RSFQ pulses transferring the comparator to an unstable state at  $I_4 = I_t$  (in the absence of signal  $I_s$  to be measured) comes to loop  $J_4$ – $J_7$ . The results of this simulation at different values of  $I_3$  for the case when either both junctions ( $I_t = 0$ ) or one ( $I_t \neq 0$ ) junction is in an unstable state are shown in Fig. 2.11 a, b, respectively. Now suppose that a single current step,  $I_s = 1(t - \tau)$ , is applied to the input of the comparator at time instant  $t = \tau$ . For a small deviation of the phase from an equilibrium value in both unstable state of the comparator, one can write a linear equation with time-varying coefficient  $G(t)$  (Askerzade and Kornev 1994a)

$$\dot{\phi}_3 + G(t)\phi_3 = \Theta(t - \tau) + i_{fb}, \quad (2.31)$$

where  $G(t) = \cos \phi_6(t)$ . In the first case of unstable equilibrium of the comparator ( $I_t = 0$ ), phase  $\phi$  is the difference between the phases of the JJs,

$$\phi = \phi_-(t) = \phi_6(t) - \phi_7(t). \quad (2.32)$$

**Fig. 2.11** Dynamics of the circuit implemented in Gudkov et al. (1988)  $I_3/I_c = 0.8$  (a) and 1.4 (b). Other parameters:  $l = 0.4$ ;  $I_1/I_c = 0.7$ ;  $\beta_C = 0.1$ ; time in units  $\hbar/2eV_c$

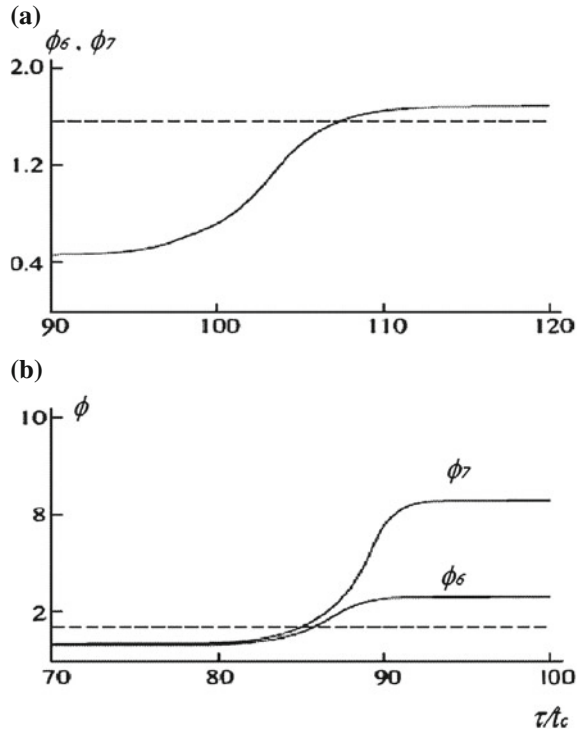
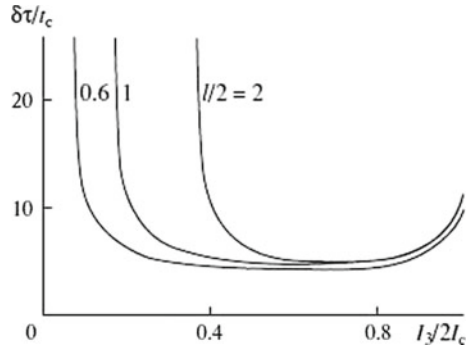


**Fig. 2.12** Time resolution of the balanced comparator based on overdamped JJ versus  $I_3/2I_c$  for different dimensionless inductance  $l$



In the second case, when  $I_t \neq 0$ , phase  $\phi$  is the difference between the actual value of phase  $\phi_6$  from the value of  $\phi_6$  calculated above (Fig. 2.11b). For the transfer characteristic, we have

$$\delta\phi = -i_{fb} = H_0^{-1} \int_{\tau}^{\infty} \exp\left(-\int_{\xi}^{\infty} G(x)dx\right) d\xi; \quad H_0 = \int_{-\infty}^{\infty} \exp\left(-\int_{\xi}^{\infty} G(x)dx\right) d\xi. \quad (2.33)$$

With expression (2.33), a family of transfer characteristics for different values of parameters  $i_3 = I_3/I_c$  and  $l = 2\pi LI_c/\Phi_0$  was calculated. This made it possible to find the dependence of the comparator's time resolution on these parameters. From Fig. 2.12, where the time resolution is plotted versus  $I_3/2I_c$  for various values of dimensionless inductance  $l$ , it follows that the minimal value of the time resolution is  $\delta\tau_{min} = 5t_c = 5\hbar/2eV_c$ . For characteristic voltage  $V_c \approx 2$  mV commonly used in the technology of LTS,  $\delta\tau_{min} = 0.8$  ps (Askerzade and Kornev 1994a).

### 2.2.7 Sensitivity of Josephson Comparators

The sensitivity of any comparator, can be determined from the switching characteristic. In the absence of fluctuations, this characteristic has a threshold character: the mean voltage across the junctions as a function of the signal amplitude has the form of an ideal step. The sensitivity of a comparator depends on a fluctuation-induced smearing of this characteristic. When the strobe pulse is rather wide, i.e., when  $\alpha \ll (3\gamma_T/2)^{2/3} < 1$  ( $\alpha$  is the dimensionless sampling rate), the smearing of the threshold characteristic of any (tunnel or hysteresis-free) JJs depends on thermal fluctuations (Askerzade 1998)

$$\frac{\Delta I_x}{I_c} \equiv \gamma_T^{2/3} \quad (2.34)$$

As follows from Eq. (2.34), the final result is independent of McCumber parameter  $\beta_C$ . This is because the Josephson phase dynamics is the same at all junctions when the sampling rate is low (Likharev 1986; Snigirev 1984). However, expression (2.34) fails in the limit of SFQ pulses, since the rate of growing of the current,  $\alpha$ , increases in this approximation, exceeding  $(3\gamma_T/2)^{2/3}$ . The dynamics and fluctuation of the delay time in this limit were studied in papers (Askerzade 1998, b). Here, of most importance is the fact that the sensitivity starts depending on rate of growing  $\alpha$  and McCumber parameter  $\beta_C$

$$\frac{\Delta I_x}{I_c} \equiv \left\{ \begin{array}{ll} 0.17\sqrt{\gamma_T}(\frac{\alpha}{\beta_C})^{3/8}, & \beta_C \gg 1 \\ 3.44\sqrt{\gamma_T}\alpha^{7/18}, & \beta_C \ll 1 \end{array} \right\}. \quad (2.35)$$

From Eq. (2.35), it follows that, when  $\alpha$  is high, the dependence of  $\Delta I_x$  on thermal fluctuation intensity  $\gamma_T$  obeys a square-root law whatever junction capacitance  $\beta_C$ . The fact is that, at a high rate of growing, fluctuations somewhat change the switching process. In both limits ( $\beta_C \gg 1$  and  $\beta_C \ll 1$ ), the threshold switching characteristic smears in proportion to rate of rise  $\alpha$  unlike time resolution  $\delta t$ . On the other hand, the smearing of this characteristic in the case of tunnel junctions is insignificant compared with overdamped junctions, since the inertia of the former is high. Because of high  $\beta_C \gg 1$ , the basic stage of switching takes an extremely short time; i.e., having gained a high velocity, a “particle” corresponding to the Josephson phase, moves “by inertia”. In general, sensitivity  $\delta I_x$  of comparators is directly proportional to smearing  $\Delta I_x$  of the threshold switching characteristic

$$\delta I_x = \frac{\Delta I_x}{\sqrt{N}}. \quad (2.36)$$

In this expression,  $N$  is an averaging factor related to the statistical character of measurement. It is equal to the number of pulses used to measure an output pattern at a time point. The value of  $N$  considerably depends on pulse repetition rate  $f$ . The maximal duration of a signal to be measured is expressed as  $\tau_{max} \leq f^{-1}$ . This means that the formula

$$N = \frac{T}{\delta t} \tau_{max} f \quad (2.37)$$

is valid if the total time of measurement of the pulse is  $T$ .

From the expressions for the time resolution, it follows that  $\delta t$  depends on characteristic voltage  $V_c$ . According to the microscopic theory (see for example Likharev 1986; Barone and Paterno 1982), the characteristic voltage is determined by the order parameter of the superconducting electrodes at a given temperature. For the highest performance LTS,  $V_c \approx 2$  mV, which corresponds to time resolution  $\delta t = 0.1$  ps in the case of RSFQ pulses. For well-known Nb based JJs,  $\delta t$  is about 1.6 ps (600 GHz) (Gubankov et al. 1983). In junctions based on HTS with critical temperature  $T_c = 90$  K, and order parameter  $\Delta_0/e = 20$  mV, characteristic voltage  $V_c$  is expected to be several millivolts at liquid nitrogen temperature  $T = 77$  K.

Bicrystalline junctions on  $SrTiO_3$  substrates were reported in Vale et al. (1997). The possibility of increasing characteristic voltage  $V_c$  to 1 mV was discussed in Poppe et al. (2001) and Divin et al. (1997). Recently in Borisenko et al. (2005), JJs have been prepared on YBCO superconductors. Here, critical current density  $j_c$  reach  $(2 - 5) \times 10^5 \text{ A/cm}^2$  at liquid nitrogen temperature and characteristic voltage is  $V_c = 0.6 - 0.9 \text{ mV}$ . The hysteresis-free IV curve of JJs on HTS makes these materials promising for designing RSFQ systems (see Chap. 3).

A HTS balanced comparator on JJs was first implemented in Sonnenberg et al. (1999). The operating frequency of that device was 72 GHz, which corresponds to a time resolution of 14 ps. In Saitoh et al. (2002), an YBCO balanced comparator was used as a component of a delta-sigma modulator. The parameters of this device were measured at an operating temperature of 20 K and an operating frequency of 100 GHz. The first YBCO sampler was implemented and then improved by Japanese scientists (Hidaka et al. 2001; Maruyama et al. 2003). The operating frequency of this sampler was equal to 120 GHz. According Eq. (2.36), sensitivity  $\delta I_x$  of Josephson comparators depends on the smearing of the threshold switching characteristic,  $\Delta I_x$ , and parameter  $N$ . The value of  $N$  strongly depends on pulse repetition rate  $f$ . In modern superconducting electronics (Likharev 2002),  $f$  on the order of 100 GHz and  $\tau_{max} \approx 10 \text{ ps}$  may be attained using electrically controlled delay line based on JJs. In this case,  $f\tau_{max} \approx 1$ . Putting  $T_m = 10^{-3} \text{ s}$  and  $\delta t \approx 1 \text{ ps}$ , we obtain  $N \approx 10^9$ . The “radiometric gain” in expression (2.37) is then  $\sqrt{N} \simeq 3 \times 10^4$ . For LTS,  $\Delta I_x$  varies from 10  $\mu\text{A}$  to 1 mA, which corresponds to sensitivity  $\delta I_x$  varying from 0.3 nA to 0.3  $\mu\text{A}$ . For HTS at liquid nitrogen temperature, we have  $\delta I_x = 1 \text{ nA}$ .

As the pulse repetition period grows, the radiometric gain decreases as (here, it is more convenient to consider  $\tau_{max}$ ). Yet, the sensitivity remains high. The value  $\delta I_x = 1 \text{ nA}$  is better than that of semiconductor samplers. The smearing of the threshold characteristic of a balanced comparator on niobium junctions was measured and analytically calculated in recent study (Walls et al. 2002) on quantum fluctuations in these devices. The data calculated in terms of the Caldeira–Leggett theory (Caldeira and Leggett 1983a) were compared with the temperature dependence of smearing  $\Delta I_x$  in the interval 1.5–4.2 K. It was found that, at higher temperatures,  $\Delta I_x$  grows as  $\sqrt{T}$ , in accordance with expression (2.35). However, as the temperature tends toward zero,  $\Delta I_x$  tends to saturate because of quantum fluctuations. It is also remarkable that  $\Delta I_x$  depends on parameter  $\beta_C$  in the quantum limit. Contrary to the prediction by expression (2.35), smearing  $\Delta I_x$  increases with  $\beta_C$  at  $T \rightarrow 0$ . Thus, balanced Josephson comparators offer a powerful means for studying quantum fluctuations in such systems (Caldeira and Leggett 1983a) and seem to be promising for investigating the properties of qubits. In closing, efforts to create LTS samplers using latching technology date back to the 1980s (Wolf et al. 1985a; Faris 1980). Hypres Co. (United States) even launched Josephson stroboscopic oscilloscopes–reflectometers in serial production (Whiteley et al. 1987). However, samplers on LTS have not found wide application, possibly because of the need to cool down the system to helium temperatures. At the same time, Japanese researchers guess that samplers made of HTS may have extensive applications, because the problem of cooling down to cryogenic temperatures here is lacking (unlike in the technology of LTS). Application

of fairly cheap many-pass nitrogen coolers to a great extent eliminates cooling-related difficulties. Note that creating superconducting samplers is also dictated by recent advances in computing facilities. These devices seem to fit naturally into digital (both semiconducting and superconducting) circuits operating at nitrogen temperatures.

## 2.3 Superconducting Interfometers and SQUIDs

This section is concerned with the basic principles underlying the devices known as SQUIDs. It is well known that such devices have opened new horizons in LTS measurement technique. A SQUID is the most sensitive measurement device which can measure magnetic flux on the order of one flux quantum  $\Phi_0$ . The magnetic properties of different systems including spin, superspin glass, and superparamagnet are studied using SQUID devices. Firstly we will discuss flux quantization in a superconducting ring with one and two JJ (single and two-junction interferometers). These interferometers used in SQUIDs as sensitive elements. Below we present details of physical foundation for operation and sensitivity of SQUIDs.

### 2.3.1 Flux Quantization in a Superconducting Ring with Single JJ

#### 2.3.1.1 Basic Equations and the Case of $0$ and $\pi$ Junctions

The basic element of a single junction interferometer is a superconducting ring containing JJ. In general, the flux on the JJ  $\Phi$  is not equal external magnetic flux  $\Phi_e$ . Their difference is due to the screening current circulating in the superconducting ring (Fig. 2.13):

$$\Phi = \Phi_e - LI_c \sin \phi. \quad (2.38)$$

For dimensionless notation we have

**Fig. 2.13** Single junction interferometer

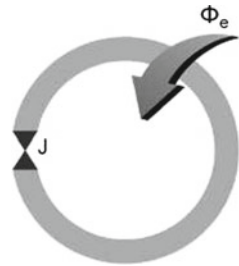
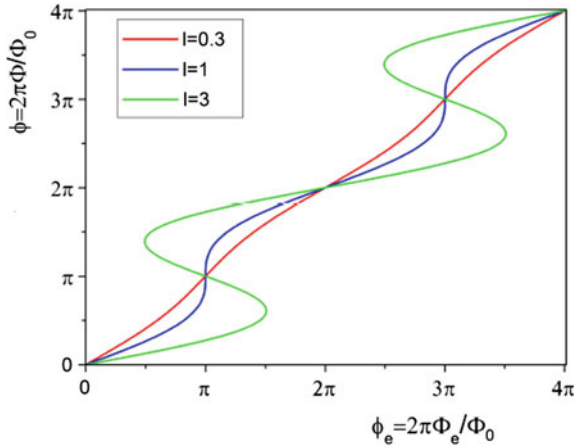


**Fig. 2.14**  $\phi(\Phi_e)$  dependence of single junction interferometer for different dimensionless inductance  $l = \frac{2\pi LI_c}{\Phi_0}$



$$\phi = \phi_e - \ell \sin \phi, \quad (2.39)$$

where external flux  $\phi_e$  in units  $\Phi_0$ ,  $\phi_e = \frac{2\pi\Phi_e}{\Phi_0}$ , dimensionless inductance  $\ell = \frac{2\pi LI_c}{\Phi_0}$ . Dependence of  $\phi(\phi_e)$  for different dimensionless inductivity parameters  $\ell$  presented in Fig. 2.14. Detail analysis behavior of single junction interferometer with junction based on s-wave superconductors and their dynamics presented in Likharev (1986), Barone and Paterno (1982).

The most interesting effect associated with  $\pi$  junction is that its sign changes in the critical current  $I_c$  of JJ, suggested by Sigrist and Rice (1992), Bulaevskii et al. (1977). It was shown that a superconducting ring containing an odd number of  $\pi$  shifts will (under certain conditions) spontaneously generate a magnetic flux  $\Phi_0/2$ . Flux quantization of a multiply connected superconductor represents one of the most fundamental demonstrations of macroscopic phase coherence in the superconducting state. For a ring with an odd number of sign changes in the circulating supercurrent  $I_s$ , it is sufficient to consider the case in which only one critical current is negative (say,  $I_s = I_c \sin(\phi + \pi)$ ). In the absence of applied magnetic field, the ground state of a superconducting ring containing an odd number of sign changes ( $\pi$  ring) has a spontaneous magnetization of a half magnetic-flux quantum (i.e.,  $I_s L = \frac{\Phi_0}{2}$ ). If the ring contains an even number of  $\pi$  shifts, including no  $\pi$  shifts at all (zero ring),  $I_s = 0$  in the ground state, and the magnetic-flux state has the standard integral flux quantization ( $\Phi = n\Phi_0$ ). Free energy of superconducting ring in general case has a form

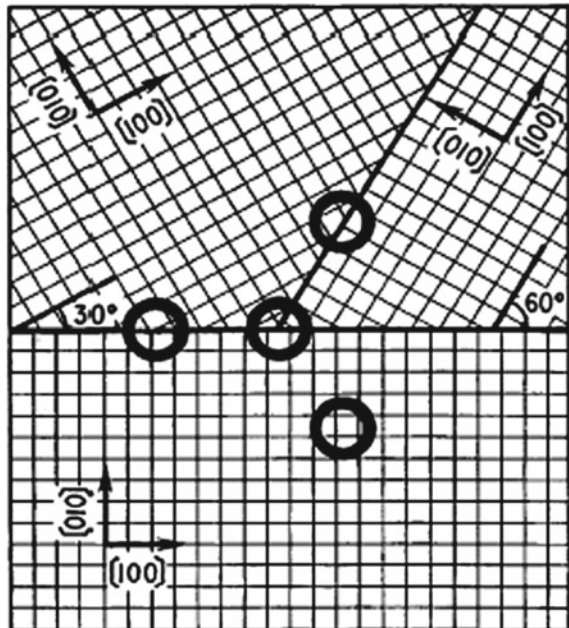
$$U(\Phi, \Phi_e) = U_L + U_S = \frac{\Phi_0^2}{2L} \left\{ (\phi - \phi_e)^2 - \frac{LI_c}{\pi \Phi_0} \cos(\phi + \varphi) \right\}, \quad (2.40)$$

where  $\varphi = 0, \pi$  for the zero ring and a  $\pi$  ring, respectively. It is well known that conventional superconductors generally tend to expel a small external magnetic

field under transition into the superconducting state. This “Meissner effect” leads to complete or (due to remnant trapped flux, e.g., in polycrystalline superconductors) partial diamagnetism. Paramagnetic “Meissner effect” was observed in ceramic  $\text{Bi}_2\text{Sr}_2\text{CaCu}_2\text{O}_8$ , which can be explained by the d-wave character of superconducting order parameter. Thus, d-wave symmetry of order parameter leads to frustrated Josephson junction circuits ( $\pi$  rings) in polycrystalline superconductors, where orientation of grains in sample seems random and contact each other.

Spontaneous generation of a with a flux  $\Phi_0/2$  at the meeting point of Josephson coupled superconducting crystals with unconventional character of pairing in a frustrated geometry was first proposed by Geshkenbein and co-workers (1986). The first experimental observation of this effect in a controlled geometry was in study (Tsuei and Kirtley 2000). In the tricrystal experiment of Tsuei and Kirtley (2000), an epitaxial YBCO film (1200 Å thick) was deposited using laser ablation on a tricrystal (100)  $\text{SrTiO}_3$  substrate with the configuration shown in Fig. 2.15. A high-resolution scanning SQUID microscope was used to direct measurement of the magnetic flux threading through HTS rings. The measurement SQUID's used were based on LTS Nb- $\text{AlO}_x$ -Nb trilayer SQUID's. Fig. 2.16 shows a scanning SQUID microscope image (Tsuei and Kirtley 2000) of a three-junction YBCO ring in the original tricrystal magnetometry experiments. Sample was cooled to 4.2 K and imaged in a magnetic field estimated to be less than  $0.4 \mu\text{T}$ . It was shown (Fig. 2.17) that the  $\Phi_0/2$  flux effect at the tricrystal meeting point persists from  $T=0.5 \text{ K}$  through

**Fig. 2.15** Experimental geometry for study of half-flux quantum state of single junction interferometer



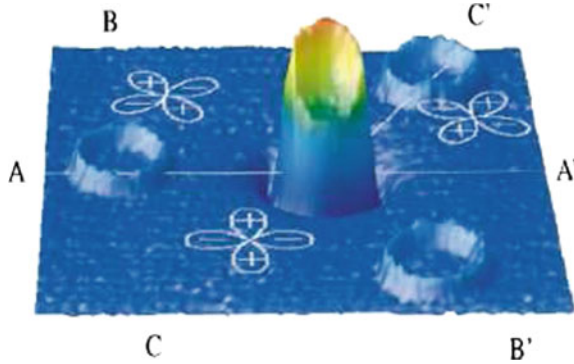
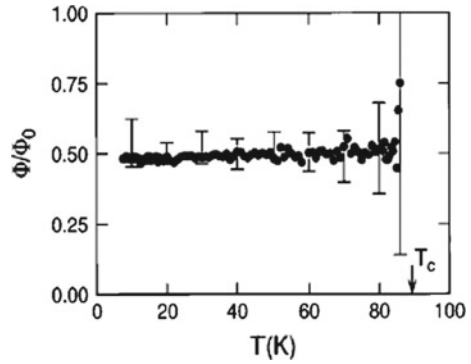


**Fig. 2.16** Three-dimensional visualization of SQUID microscope image of a thin-film YBCO tricrystal ring sample, cooled and imaged in nominally zero magnetic field (Kirtley 2010)

**Fig. 2.17** Frustrated state of tricrystal geometry as function of temperature (Kirtley 2010)



$T_c = 90$  K) with no change in total flux ( $\Phi_0/2$ ). It means that d-wave symmetry of superconducting state dominates in HTS (Kirtley 2010). This implies that the three outer control rings have no magnetic flux trapped in them, but in the three-junction ring at the center has  $\Phi_0/2$  total flux. Visualization of the control rings are related with a slight change in the inductance of the SQUID.

### 2.3.1.2 Effects of Fluctuations on a Single-Junction Interferometer

Calculation of average value of the Josephson term  $\langle U_S \rangle$  in Eq. (2.40) for  $\phi_e = 0$  yielded to Khlus and Kulik (1975)

$$\langle U_S \rangle = -E_J \cos \langle \phi \rangle \exp \left( -\frac{L}{L_{F0}} \right), \quad (2.41)$$

where  $L_{F0}$  is the so called “thermal fluctuational” inductance determined as



$$L_{F0} = \left( \frac{\Phi_0}{2\pi} \right)^2 \frac{1}{kT}. \quad (2.42)$$

For  $L > L_{F0}$ , the Josephson interference is sharply suppressed by thermal fluctuations. This fact imposes limitations on the ring size in a superconducting single junction interferometer. For helium temperatures it corresponds to the value about 2 nH, which restrict using superconducting rings about 1 mm. At very low temperatures, an important role belongs to quantum fluctuations. Influence of quantum fluctuations on single-junction interferometer considered in Askerzade (2005a). For low inductance interferometers ( $\ell \ll 1$ ), the matrix element of the superconducting current in the ground state is given by the expression

$$\langle 0 | I_c \sin \phi | 0 \rangle = -\frac{2\pi E_J}{\Phi_0} \sin \phi_e \exp(-L/L_{FQ}), \quad (2.43)$$

where  $L_{FQ} = (\frac{\Phi_0}{\pi})^2 \frac{1}{\hbar\omega}$  and the frequency  $\omega$  is determined as  $\omega = \frac{1}{\sqrt{LC}}$ , where  $L$  is the inductance of superconducting loop,  $C$  is the capacitance of JJ. It means that above presented result given by expression (2.41) remains in power in the case of low inductance interferometers, however by replacing the thermal energy  $kT$  with the energy of quantum  $\hbar\omega$ . In the case of a high inductance at low temperatures as in a single junction Josephson interferences is suppressed (Askerzade 2005a).

### 2.3.2 Basic Schema of AC SQUID and Their Parameters

Schematic representation of AC SQUID presented in Fig. 2.18. A current of frequency  $\omega$  is supplied by a high-impedance AC current source to the resonance circuit (Zimmerman et al. 1970) and (Mercereau 1970). Detailed review of of operation of

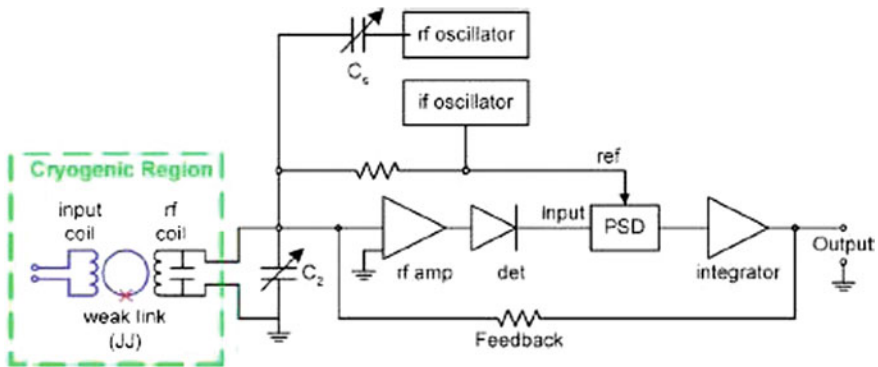


Fig. 2.18 Basic schema of AC SQUID

AC SQUIDS have been written by many authors (Danilov et al. 1980; Clarke 1996; Chesca 2004). Frequencies  $\omega$  is usually 10–30 MHz, however there are AC SQUIDS operating at GHz. The coil of the resonant circuit is coupled to the superconducting loop of a single junction interferometer. The AC voltage across the tank circuit is magnified by the amplifier. The device input is the coil inductively coupled to the SQUID loop. Historically, it appears that most LTS AC SQUIDS were operated in the hysteretic mode, although it was shown that, there are advantages to the nonhysteretic mode. For this reason, the importance of the nonhysteretic AC SQUID was not widely exploited experimentally. In relation with discovery of HTS has changed this situation dramatically, due to the systematic experimental study of the Germany group from Julich.

### 2.3.2.1 Hysteretic Mode

First important characteristic of the AC SQUID is the transfer coefficient  $H$  of the applied flux  $\Phi_x$  on the output voltage  $V$ . As shown by theoretical analysis in study (Danilov et al. 1980), in the case of hysteretic mode, i.e. high inductance ( $\ell \gg 1$ ) interferometers transfer coefficient  $H$  for AC SQUIDS can be written as

$$H = \left| \frac{\partial V}{\partial \Phi_x} \right| = \frac{\omega_T}{k} \sqrt{\frac{L_T}{L}}; \quad k = \frac{M}{\sqrt{LL_T}}, \quad (2.44)$$

where  $L_T$  is the inductance of tank circuit and  $\omega_T$  is a tank frequency. In last expression inductive coefficient  $k$  should be greater than  $Q_T^{-1/2}$ , where  $Q_T$  is the quality factor of the tank circuit (see Fig. 2.18). Estimation of transfer coefficient  $H$  for AC SQUIDS leads to results  $10 \mu\text{V}/\Phi_0$ . Another characteristic of the SQUIDS is the energy sensitivity, which is determined as

$$E_V = \frac{(\delta\Phi_x)^2}{2L\Delta f}, \quad (2.45)$$

where  $\delta\Phi_x$  is the magnetic flux at the level noise of SQUID in the frequency interval  $\Delta f$ . Estimation of energy sensitivity  $E_V$  of AC SQUID gives result at the level  $5 \times 10^{-29} \text{ J/Hz}$ , in which we take into account for interferometer inductance the value  $L = 3 \times 10^{-10} \text{ H}$ . The corresponding intrinsic flux noise of the AC SQUID calculated in the study (Kurkijarvi 1973) and is given by the expression

$$S_\Phi^i(f) = \frac{(LI_c)^2}{\omega_T} \left( \frac{2\pi kT}{I_c \Phi_0} \right)^{4/3}. \quad (2.46)$$

### 2.3.2.2 Nonhysteretic Mode

For low inductance interferometers ( $\ell \ll 1$ ) the operation of the nonhysteretic AC SQUID were described (Likharev 1986; Hansma 1973; Ryhanen et al. 1989). For low inductance interferometers ( $\ell \ll 1$ ), the total magnetic flux threading the SQUID is nearly equal to the applied flux, and  $\omega_T = \frac{L_R}{\Phi_0}$ . The transfer coefficient in this regime can be written as

$$H = \frac{2}{\pi} \kappa^2 Q l \frac{\omega_T}{k} \sqrt{\frac{L_T}{L}}. \quad (2.47)$$

This transfer coefficient exceeds that of the hysteretic AC SQUID by a factor of order  $\kappa^2 Q l$ , which can be made larger than unity for the nonhysteretic case by choosing  $\kappa^2 Q \gg 1$ . The intrinsic noise energy of LTS, nonhysteretic, AC SQUIDS has been calculated by several authors, and is approximately

$$E_V = \frac{3kT}{\ell^2 \omega_c}. \quad (2.48)$$

In derivation of last expression the external frequency is set equal to cutoff frequency of SQUID  $\omega_c = L/R_N$  and thermal fluctuations considered as perturbation  $\gamma_T = \frac{kT}{E_J} \ll 1$ . This is generally much lower than for the hysteretic mode. An energy sensitivity in this mode at the level of  $20\hbar$  (Kuzmin et al. 1985). The intrinsic energy sensitivity remains low even in the large fluctuation  $\gamma_T > 1$ . Optimized value of dimensionless inductance is  $\ell = 1/\gamma_T$  (Chesca 1998). As a result, nonhysteretic AC SQUID can be operated with relatively large inductance and hence large effective area, increasing their sensitivity.

Value of energy sensitivity  $E_V$  for different types of SQUIDS is considerably different. AC SQUIDS are characterized by the high value of noise sensitivity  $E_V$ . AC SQUIDS has simple construction in comparison with DC SQUID. However, using AC current for measurements causes additional complication in application. High value of  $E_V$  is not determined by fundamental fluctuations in single junction interferometer and depends noises of AC SQUID amplifier (Koelle et al. 1999). The overall noise energy of the hysteretic AC SQUID should not increase very much as the temperature is raised from 4 K to 77 K. However, it should be noted that there are no simulations or calculations to the best of our knowledge in this respect. In the case of DC SQUID, the overall noise energy will increase significantly as the temperature is raised to 77 K (Koelle et al. 1999) since a properly designed circuitry is limited largely by intrinsic noise at 4.2 K. The energy sensitivity of different types of SQUIDS as function of frequency presented in Fig. 2.19 (Fagaly 2006).

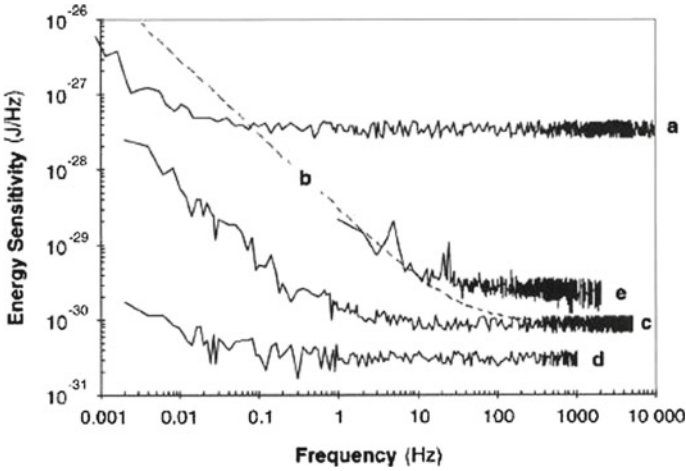


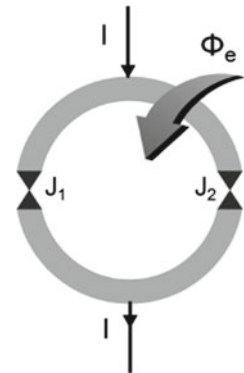
**Fig. 2.19** Energy sensitivity of SQUIDs versus frequency for different SQUID device. a is a LTS AC SQUID operated at a bias frequency of 19 MHz; b is a DC biased LTS DC SQUID with amorphous silicon barriers; c is b using AC biasing; d is a DC biased LTS DC SQUID with AlOx barriers; and e is an AC biased HTS DC SQUID utilizing a ramp edge junction. Devices a–d were operated at 4.2 K; device e was at 77 K (Fagaly 2006)

### 2.3.3 Double Junction Interferometer and DC SQUID

#### 2.3.3.1 JJs Based on S-Wave Superconductors

Two-junction interferometer consists of two JJs in parallel, forming a superconducting ring (Fig. 2.20). Suppose that a magnetic flux  $\Phi$  passes through the interior of the loop. Equations describing the double junctions interferometer dynamics can be regarded as an equation of motion of a point mass in a field of force with a 2D potential

**Fig. 2.20** Double junction interferometer



$$\frac{U(\phi_1, \phi_2)}{2E_J} = \frac{\pi}{\ell} \left( \frac{\phi_1 - \phi_2}{2} - \frac{\Phi}{\Phi_0} \right)^2 + \frac{i}{2} \pi \frac{\phi_1 + \phi_2}{2} - \cos \pi \frac{\phi_1 + \phi_2}{2} \cos \pi \frac{\phi_1 - \phi_2}{2}, \quad (2.49)$$

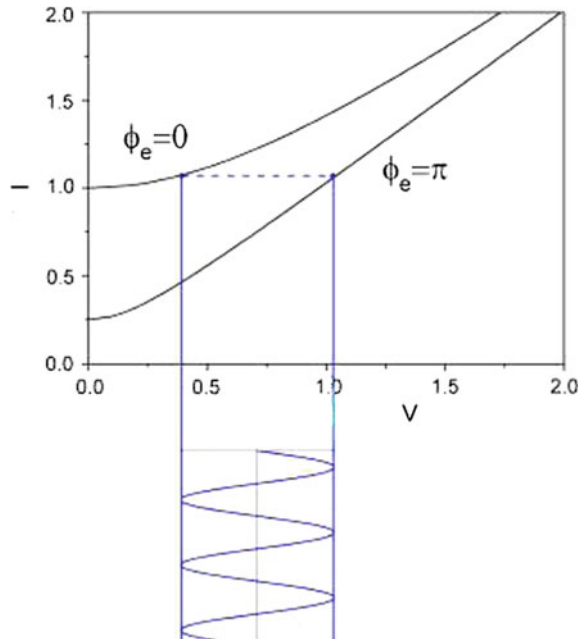
where  $\ell$  is the normalized total inductance of double-junction interferometer,  $\phi_i$   $i = 1, 2$  is the phase of JJ ( $J_1$  and  $J_2$ ). As shown by simulations, for  $i = 0.4$ ,  $U(\phi_1, \phi_2)$  has multiple metastable state separated by saddle points on the  $\phi_2 = \phi_1$  line. By increasing bias current  $I$ , these saddle points gradually disappear. At  $I > I_c$  it seems that all the saddle points disappear, suggesting no stable state corresponding to local minima of the potential energy. Detail description of double-junction interferometers on conventional superconductors were presented in Likharev (1986) and Barone and Paterno (1982).

In the case of double-junction low inductance interferometers ( $\ell \ll 1$ ) total current can be written as

$$I = 2I_c \sin(\phi_1 - \pi \phi_e) \cos \pi \phi_e. \quad (2.50)$$

It means, that the critical current of double junction interferometer in this limit is a periodic function of the external magnetic flux. Ideal case for the  $I/I_c$  versus  $\Phi_{ext}/\Phi_0$  curve in the double junction interferometer, where  $I$  is the maximum super-current  $I_{\max} = 2I_c |\cos \pi \phi_e|$ .  $I = 2I_c$  when  $\Phi_{ext}/\Phi_0 = n$  (integer) and  $I = 0$  for  $\Phi_{ext}/\Phi_0 = n + 1/2$ . Voltage variation across the two-junction interferometer resulting from modulation of the maximum zero-voltage current by an externally applied flux through the superconducting loop also presented in Fig. 2.21.

**Fig. 2.21** IV curve of two junction interferometer under external magnetic field



### 2.3.3.2 JJs Based on D-Wave Superconductors

The predominantly  $d_{x^2-y^2}$  symmetry of the order parameter (see Chap. 1) in HTS influences fundamental properties of JJs and superconducting interferometers. We consider two-junction  $\pi$  interferometers which consist of one JJ with negative critical current (Harlingen 1995). In papers (Chesca et al. 2002; Chesca 1999), the theories describing the effects of LC resonances on the IV curve of conventional interferometers have been extended, accounting for a possible complex mixed symmetry  $\varepsilon s + i(1 - \varepsilon)d_{x^2-y^2}$ ,  $0 < \varepsilon < 1$  of the order parameter. Experimental realization and notation of a  $\pi$  two-junction interferometer presented in Fig. 2.22 (Chesca et al. 2002). The detail analysis (Chesca 1999) predict  $d_{x^2-y^2}$ -wave induced zero-field current enhancements due to resonances to appear in the IV curve of  $\pi$  interferometers with small JJs (Chesca et al. 2002). The self-induced resonances occurring in two-junction  $\pi$  interferometers have been observed at temperatures of 4.2–77 K (Fig. 2.23) (Chesca et al. 2002). These resonances reveal that the  $d_{x^2-y^2}$  wave symmetry induces in zero applied magnetic field circulating AC currents, which oscillate with Josephson frequency  $\omega_J$ . The high frequency behavior of  $\pi$  interferometers provides an evidence to complement the behavior of ordinary two-junction interferometer. Experimentally proved that the  $\pi$  shift observed before in the zero-voltage state is present for Josephson frequencies up to several tens of GHz (Chesca et al. 2002).

**Fig. 2.22**  $\pi$  two-junction interferometer

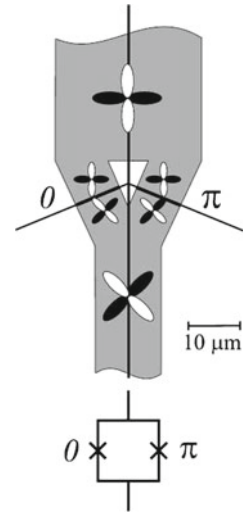
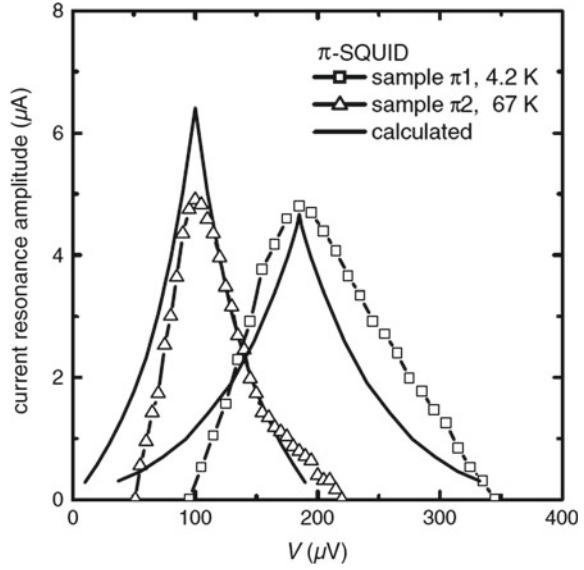


**Fig. 2.23** Zero-field resonance as function of voltage in  $\pi$  two-junction interferometer (Chesca et al. 2002)



### 2.3.4 DC SQUID Characteristics

The scheme of DC SQUID presented in Fig. 2.24 contains as sensitive element double-junction interferometer. The unique sensitivity of the DC SQUIDS can be used in some situations where a variation of the quantity of interest can be transformed into variation of magnetic flux. Detail analysis of operation of DC SQUIDS presented in books (Likharev 1986; Barone and Paterno 1982) and in the review papers (Koelle et al. 1999; Fagaly 2006). The transfer coefficient  $H$  of the output voltage  $V$  on the applied flux  $\Phi_x$  for DC SQUIDS is very high in comparison AC SQUIDS and can reach the value  $1\text{mV}/\Phi_0$ . For this reason amplifier noise is negligible small in comparison with intrinsic fluctuations in double junction interferometer. For DC SQUIDS with small inductance  $\ell \ll 1$  (Likharev 1986; Barone and Paterno 1982), the transfer coefficient  $H$  given by expression

$$H = \frac{\omega_c I_{c1} I_{c2} \sin \phi_e}{\ell_{c+}^2 v}, \quad (2.51)$$

where  $\ell_{c+} = \ell_{c1} + \ell_{c2}$  is the normalized total inductance of superconducting loop and  $v = \frac{V}{V_c}$  is the normalized voltage in double-junction interferometer.

For DC SQUIDS with high inductance  $\ell \gg 1$ , transfer coefficient  $H$  can be written as

$$H = \frac{\omega_c \Phi_0}{2\pi L_+ I_{c1} v}, \quad (2.52)$$

where  $L_+ = L_1 + L_2$  is the total inductance of superconducting ring.

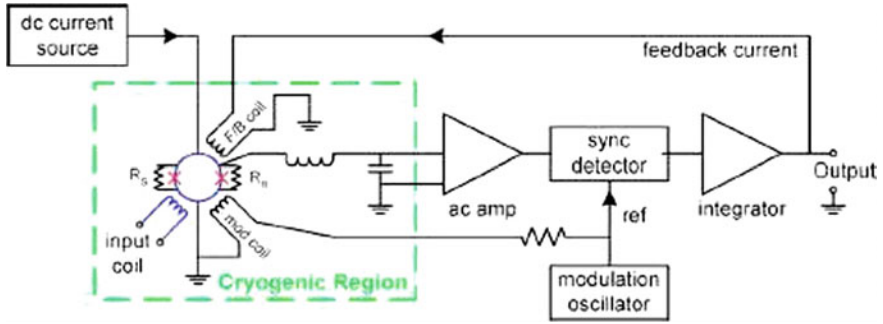


**Fig. 2.24** The scheme of DC SQUID

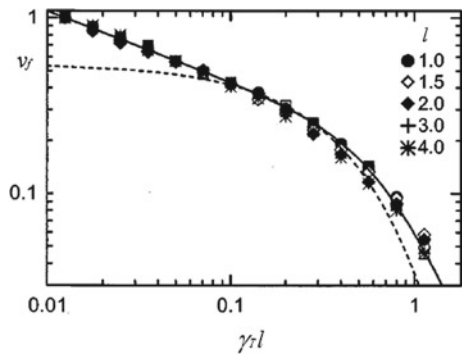
As shown in Koelle et al. (1999), on calculating the dimensionless transfer coefficient  $v_f = H\Phi_0/I_c R_N$  versus  $\gamma_T \ell$  for values of  $\ell$  ranging from 0.6 to 4 one finds that, although  $v_f$  for a given value of  $\gamma_T \ell$  decreases with  $\ell$ , its functional dependence on  $\gamma_T \ell$  is essentially the same for all values of  $\gamma_T \ell$ . Thus, on normalizing curves of  $v_f$  versus  $\gamma_T \ell$  to their value at, say,  $\gamma_T \ell = 1/80$ , one obtains a universal curve which is independent  $\ell$ . Note that the value of  $\gamma_T \ell = 1/80$  is an arbitrary but convenient choice suggested by the smallest value of  $\gamma_T \ell = 1/80$  used in the simulations (Fig. 2.25). The solid and dashed lines in Fig. 2.25 corresponds to different empirical expressions for fitting (Koelle et al. 1999).

It means that energy sensitivity of DC SQUIDs is determined by the characteristics of JJs. In the case of small thermal fluctuations  $\gamma_T \ll 1$ , theoretical analysis gives result for  $l \simeq 1$  energy sensitivity (Likharev 1986; Koelle et al. 1999; Kleiner et al. 2004)

$$(E_V)_{\min} = \frac{9kT}{\omega_c}. \quad (2.53)$$

More generally, in the limit  $\gamma_T l < 0.2$  one finds (Likharev 1986; Koelle et al. 1999; Kleiner et al. 2004)

**Fig. 2.25** Transfer function  $H$  of DC SQUIDs as function of  $\gamma_T \ell$  for  $\beta_C = 0.5$  (Koelle et al. 1999)





$$(E_V)_{\min} = \frac{2(1 + \ell)\Phi_0 kT}{I_c R_N}. \quad (2.54)$$

As followed from last expression, energy sensitivity  $(E_V)_{\min}$  increases with temperature, for optimized parameters, scales as  $1/I_c R_N$ . For LTS based high quality JJ with area  $1 \mu\text{m}^2$  and critical current density  $j_c = 10^3 \text{ A/sm}^2$  plasma frequency  $\omega_p$  at the level  $10^{12} \text{ s}^{-1}$ . Using this data gives result for  $(E_V) = 0.6 \times 10^{-33} \text{ J/Hz}$ . In the study (Koelle et al. 1999) experimentally was achieved result close to this value. Energy sensitivity versus frequency for DC SQUIDs also presented in Fig. 2.19. It is clear that energy sensitivity of DC SQUIDs 10 times better than AC SQUIDs.

## 2.4 Superconducting Microwave Devices

In a superconductor, resistance is zero for DC current and the current flows without any dissipation. However, for AC current, superconductor shows a resistance, although the value of the resistance is very small. A phenomenological two-fluid model of superconductivity has been used to explain the general behavior of superconductors at AC external field. Two-fluid relation for the complex conductivity (Tinkham 1996; Van Duzer and Turner 1981), lead to the expression for surface impedance of superconductor

$$Z_s = R_s + jX_s, \quad (2.55)$$

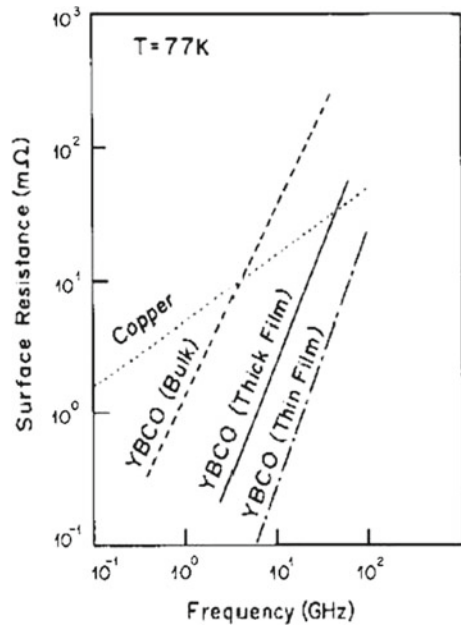
where  $R_s$  and  $X_s$  are real and imaginary parts of the impedance, respectively:

$$R_s = \frac{\mu_0^2 \omega^2 \lambda_L^3 n_n e^2 \tau}{2m}, \quad (2.56)$$

$$X_s = \omega \mu_0 \lambda_L. \quad (2.57)$$

In last equations  $m$  is the effective mass of the charge carriers,  $\tau$  is the scattering time for quasiparticle,  $\lambda_L$  is the London penetration depth,  $\omega$  is the angular frequency, and  $\mu_0^2$  is the vacuum permeability. The total carrier density is the sum of superconducting and normal state densities  $n = n_s + n_n$ . The surface resistance  $R_s$  for a superconductor is proportional to the square of the frequency, whereas for a normal conductor, the surface resistance is proportional to the square root of the frequency. Both components of surface impedance of a superconductor play an important role in determining the performance of microwave devices and filters. The real part of surface resistance  $R_s$  determines the quality factor  $Q$  of the resonator, whereas the reactive component  $X_s$  determine the sensitivity to temperature variation of the wavelength of a transmission line and the long-term stability of the device.

**Fig. 2.26** Surface resistance versus frequency in YBCO (Button et al. 1996)



The measurement of surface resistance of superconductors is important in order to determine the suitability for its application in microwave devices. Figure 2.26 shows variation of the surface resistance with the microwave frequency for HTS YBCO bulk, thick, and thin films (Button et al. 1996). The variation of surface resistance of copper is also shown in Fig. 2.26 for comparison. The surface resistance of YBCO is lower than the surface resistance of copper for the frequency  $f^*$ , where  $f^*$  is the crossover frequency. The value of  $f^*$  is highest for the YBCO thin film. The surface resistance of the YBCO thin film is minimum in comparison to YBCO bulk and thick films.

### 2.4.1 Resonators

Superconducting resonators have been fabricated in a three-dimensional structure (cavity, dielectric resonator) and in a planar structure. Fundamental characteristics of resonators can be determined by quality factor  $Q$  and given by an expression (Barone and Paterno 1982)

$$Q = \frac{f_0}{\Delta f}, \quad (2.58)$$

where  $f_0$  is the resonance frequency and  $\Delta f$  is the 3 dB frequency bandwidth of the resonator response. Prior to the discovery of HTS, planar structure resonators based

on conventional metals had limited use due to its low  $Q$  value. The low value of the surface resistance of HTS has made it possible to realize high- $Q$  planar resonators (Lancaster et al. 1990; Button and Alford 1992). For a *YBCO* thick-film cavity resonator operating at 5.66 GHz in *TE*<sub>011</sub> mode, the  $Q$  value of 715,688 at 77 K has been demonstrated in Button and Alford (1992). A number of another type HTS helical resonators have been built and tested in studies (Porch et al. 1991; Peterson et al. 1989). These have been made from either thick-film or bulk polycrystalline material. A *YBCO* wire-based helical resonator has been fabricated that showed a  $Q$  of 16,000 at 77 K and an operating frequency of 355 MHz (Peterson et al. 1989).

### 2.4.2 Filters

One of the important components of microwave circuits are the filters. In addition to conventional applications, filters are used as a matching networks as a part of multiplexers and amplifiers. Resonators are the most common basic elements used for making filters. The main requirements for the resonators that can be used for filters are a high quality factor as well as high power handling capability. Different types of HTS based filters have been fabricated and tested in Mansour et al. (2000). These include 3D structure using dielectric resonators and 2D planar structure fabricated using HTS thin films. In study (Mansour et al. 2000) dielectric resonator–HTS based film filters have been shown to handle extremely high power levels in the range 50–100 W.

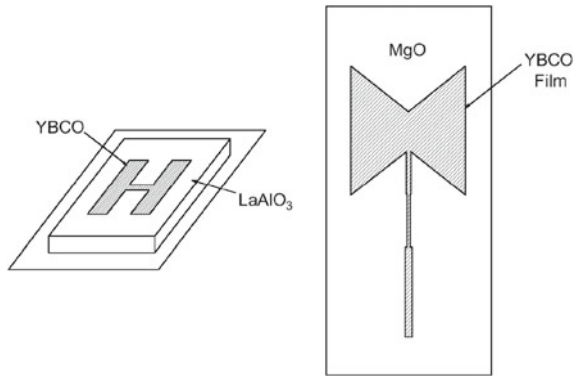
### 2.4.3 Antenna

Superconducting material may significantly improve the performance of an antenna or an antenna system such small antennas, matching circuits, superdirective arrays (Hansen 1990). Some of the applications were considered in study (Lancaster et al. 1992). The radiation efficiency  $\eta$  of a short antenna is determined by the expression

$$\eta = \frac{R_r}{R_r + R_l}, \quad (2.59)$$

where  $R_l$  is the ohmic loss resistance,  $R_r$  is the radiation resistance of antenna. Using HTS material in place of a normal conductor leads to an increase of the efficiency due to the smaller value of  $R_l$  (Khare 2003). Figure 2.27 is a schematic of HTS loop antenna, “H”-type patch (Chaloupka et al. 1991), and triangular patch antenna, along with the dipole antenna (Chung 2001). The high value of  $Q$  and small substrate height in HTS based antenna results in a narrow bandwidth between 0.85 and 1.1%. An increase of substrate height can broaden the operation bandwidth of an antenna. However, the thickness of the substrate is restricted by critical value (Khare 2003).

**Fig. 2.27** Schematic description of HTS antenna



### 2.4.4 Delay Lines

Delay lines are useful devices in electronic warfare systems, satellite communication systems, and in realizing transversal filters for analog signal processing applications. Typical delays needed for satellite communication systems are in the range of 100–300 ns. Traditional technologies for delay lines include surface acoustic wave devices and transmission coaxial cables in the form of a coil. Superconducting delay lines offer the highest bandwidth with much lower insertion loss in a highly compact design. Several HTS planar transmission lines such as stripline, microstrip, and coplanar lines could be used to realize delay lines. Using YBCO thin film deposited on both sides of a 50-mm-diameter, 25- $\mu$ m-thick LaAlO<sub>3</sub> wafer, a nondispersive delay line with 20 GHz of bandwidth has been fabricated that produces a delay of 22.5 ns with an insertion loss of 5 dB (Talisa et al. 1995).

## 2.5 Superconducting Devices in Meteorology

### 2.5.1 Voltage Standards

Physical foundation of operation voltage standard related with Shapiro steps in IV curve of externally radiated JJ (Shapiro 1963). It is well known that Shapiro steps in IV curve arises in voltages

$$V_n = n \frac{\hbar\omega}{2e}. \quad (2.60)$$

Due to that frequency can be measured with high accuracy  $\delta\omega \sim 10^{-14}$ , Josephson voltage standards allows to control voltage with the same accuracy. Traditional voltage standards use complex comparator schemes, due to small jumps of current at high voltages (Dziuba et al. 1974). Using integral circuit technology (Niemeyer

et al. 1986) gives possibility to get serial connecting about  $N \sim 1000$  of JJs and as result reaching of output voltage at the level 1 V. In this approach accuracy of voltage standard reach the value  $\delta V \sim 10^{-10}$  V. A new programmable Josephson voltage standard first proposed and fabricated by Hamilton et al. (1989) ensures fast step selection and inherent stability. This type of voltage standard is based on a binary sequence of series arrays of overdamped JJs. The IV curve remains single-valued even under microwave radiation. This allows the voltage step to be rapidly selected by just applying the DC bias current to the appropriate array sections. Moreover, the larger step width provides greater stability against different type of noises.

Voltage standards with accuracy at the level of fundamental constants have been realized with binary sequences of overdamped Josephson Junctions (Schulze et al. 2000). In the study Schulze et al. (2000) circuit complexities reached the level of 70,000 large area JJs ( $8 \times 50 \mu m^2$ ) for using in voltage standard circuits. A 10 V constant voltage was obtained under 70 GHz microwaves with power less than 1 mW. This microwave could be propagated by coupling of Josephson oscillations of all junctions which was distributed over 64 parallel microwave parts. A new circuit for JJ voltage standards was reported by Schubert et al. (2002). In these circuits coplanar strips are used for integration of the Josephson junction into a transmission line. 10 V Josephson voltage standard was realized using circuits coplanar strips design with 17,000 tunnel junctions. At frequencies around 70 to 75 GHz these standard generate reliable quantized voltage steps at 10 V with a current-step-width of about  $20 \mu A$  (Schubert et al. 2002).

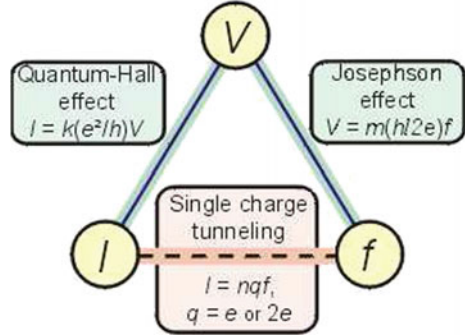
### 2.5.2 Current Standards

The small-area Josephson junctions with nano dimensions operating on the principle of Coulomb blockade of single electrons and Cooper pairs are today very important for current standard (Likharev and Zorin 1985; Nakamura et al. 1999; Zorin 2006). A deterministic current of individual charge carriers flowing through the pump under an AC drive of frequency  $f$ , can be presented as (Lotkhov et al. 2001)

$$I = ef \quad (2.61)$$

with an accuracy of  $10^{-8}$ , can be used for the electrical current standard (Lotkhov et al. 2001). Significant improvement of the quantum standard of current can be obtained transferring Cooper pairs instead of electrons (Niskanen et al. 2003). Increase of the pumping current in single-charge devices up to the level of 1 nA can impact the quantum meteorology of electrical units. With the increase of pumping current,

**Fig. 2.28** The solid state based meteorological triangle (Brake et al. 2006)



cryogenic current comparators provide accurate comparison of currents. Finally, this means completion of the meteorological triangle (Piquemal and Geneves 2000), shown in Fig. 2.28 (see also Brake et al. 2006).

## 2.6 Multi-terminal Devices

The multi-terminal Josephson Junctions generalizes the ordinary Josephson Junctions to the case of weak coupling between several superconducting terminals (Amin et al. 2002). Compared with two-terminal junctions, such systems have additional degrees of freedom. It means that there are corresponding set of control parameters, preset transport currents and applied magnetic fields. One of the possible realizations of a multi-terminal Josephson junction the set of superconducting terminals in which a common center connected with the microbridges. Realizations of such a coupling is the system shown in Fig. 2.29a. Another type of multiterminal JJ is based on the weak coupling of bulk superconductors through the two-dimensional normal layer (Fig. 2.29b). In four-terminal junction the non-local coupling of supercurrents is established due to the phase-dependent local Andreev reflections inside the weak link (de Bruyn 1999). The properties of the weak superconducting junction are described by the CPR (The total current in each terminal as function of the phases of the order parameter in the terminals). The CPR for the structure of Fig. 2.29a can be easily obtained by solving the GL equations close to temperatures  $T \sim T_c$  and the lengths of bridges  $d_j$  much smaller then the coherence length  $\xi(T)$ . The supercurrent flowing into the  $j$ th terminal is determined by the phases of the superconducting order parameter  $\phi_k$  in all the terminals (de Bruyn 1999).

$$I_j^s = \frac{\pi \Delta_0^2(T)}{4ekT_c} \sum_k \gamma_{jk} \sin(\phi_j - \phi_k), \quad (2.62)$$

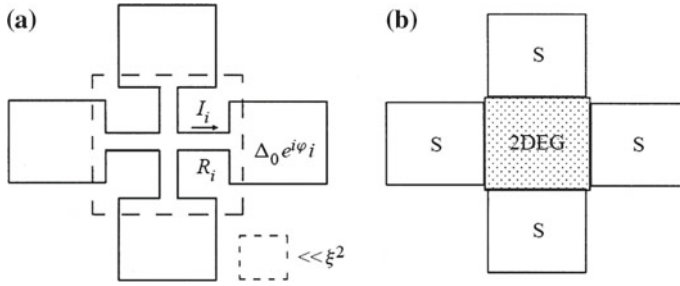


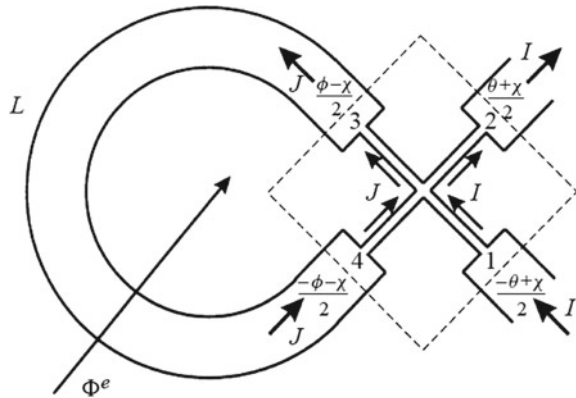
**Fig. 2.29** The superconducting four-terminal JJ (a); the mesoscopic four-terminal JJ (weak coupling of bulk SC with two-dimensional electron gas)

where  $\Delta_0^2(T)$  is the gap in the banks,  $\gamma_{jk}$  are the coefficients of coupling. The nonstationary regime can be qualitatively studied in the frame of the RSJ model (Likharev 1986), i.e. to the supercurrent we add the normal current  $I_j^n = V_j/R_j$ . The state of multiterminal JJ is described by the dynamic variables, the phases  $\phi_j$  of the superconducting order parameter in the terminals. Let us consider the particular case of four terminals. Without loss of generality we can put  $\sum_k \phi_k = 0$ . Thus, it is convenient to introduce new variables for four terminal devices (de Bruyn 1998; Vleeming et al. 1999) as shown in Fig. 2.30

$$\theta = \phi_1 - \phi_2; \quad \phi = \phi_3 - \phi_4; \quad \chi = \frac{1}{2}(\phi_1 + \phi_2) - \frac{1}{2}(\phi_3 + \phi_4). \quad (2.63)$$

The four-terminal interferometer is a novel superconducting device, which is based on a four-terminal JJ. It exhibits quantum behavior by combining the properties of a single current-biased Josephson weak link and a superconducting ring interrupted by a JJ. A schematic drawing of an four terminal interferometer is given in Fig. 2.30.  $I$  is the transport current running from terminal 1 to terminal 2. The processes of switching

**Fig. 2.30** The four-terminal interferometer  $\phi = \phi_3 - \phi_4$ ,  $\chi = (\phi_2 + \phi_1)/2 - (\phi_3 + \phi_4)/2$ ,  $\theta = \phi_2 - \phi_1$



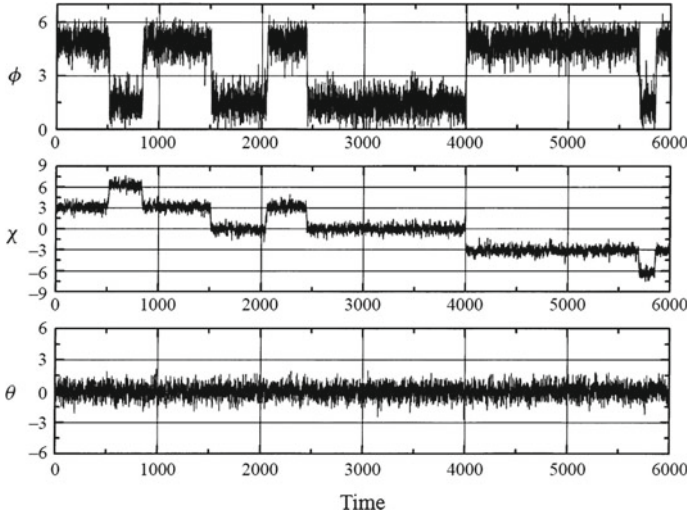


**Fig. 2.31** The three phase differences  $\phi$ ,  $\chi$ ,  $\theta$  versus time in the presence of noise (for parameters see Vleeming et al. 1999)

in the bistable state, produced by the thermal noise, were studied numerically in by solving corresponding equations and observed in experiments (Vleeming et al. 1999). Figure 2.31 display some typical results, obtained by numerical simulation. In bistable state produced transition between both flux state. Jump in  $\phi$  are accompanied by jumps in  $\chi$  by  $\pm\pi$ . At zero transport current no switching in  $\theta$  occurs.



Modern Aspects of Josephson Dynamics and  
Superconductivity Electronics

Askerzade, I.; Bozbey, A.; Cantürk, M.

2017, XVI, 186 p. 161 illus., 66 illus. in color., Hardcover

ISBN: 978-3-319-48432-7